

Superconductivity Proximate to Non-Abelian Fractional Spin Hall Insulator in Twisted Bilayer MoTe₂

Cheong-Eung Ahn,^{1,*} Donghae Seo,^{1,*} Gyeoul Lee,² Youngwook Kim,³ and Gil Young Cho^{4,5,†}

¹*Department of Physics, Pohang University of Science and Technology, Pohang, 37673, Republic of Korea*

²*Department of Physics, Ulsan National Institute of Science and Technology, Ulsan 44919, Republic of Korea*

³*Department of Physics and Chemistry, Daegu Gyeongbuk Institute of Science and Technology (DGIST), Daegu 42988, Republic of Korea*

⁴*Department of Physics, Korea Advanced Institute of Science and Technology, Daejeon 34141, Republic of Korea*

⁵*Center for Artificial Low Dimensional Electronic Systems, Institute for Basic Science, Pohang 37673, Korea*

Twisted bilayer MoTe₂ near two-degree twists has emerged as a platform for exotic correlated topological phases, including ferromagnetism and a non-Abelian fractional spin Hall insulator. Here we reveal the unexpected emergence of an intervalley superconducting phase that intervenes between these two states in the half-filled second moiré bands. Using a continuum model and exact diagonalization, we identify superconductivity through multiple signatures: negative binding energy, a dominant pair-density eigenvalue, finite superfluid stiffness, and pairing symmetry consistent with a time-reversal-symmetric nodal extended *s*-wave state. Remarkably, our numerical calculation suggests a continuous transition between superconductivity and the non-Abelian fractional spin Hall insulator, in which topological order and symmetry evolve simultaneously, supported by an effective field-theory description. Notably, our field-theoretic analysis indicates that superconductivity is driven by the condensation of charge-*e*/2 self-bosonic non-Abelian anyons, thereby providing a concrete realization of anyon superconductivity. Complementarily, when approached from the normal metallic side, superconductivity instead emerges from a Kohn–Luttinger instability enabled by the non-uniform quantum geometry of the flat moiré bands. Our results establish higher moiré bands as fertile ground for intertwined superconductivity and topological order, and point to experimentally accessible routes for realizing superconductivity in twisted bilayer MoTe₂.

Introduction

Flat topological bands with strong electron correlations have recently attracted significant attention for realizing long-sought topological phases [1–5], such as fractional Chern insulators [6–18], which are promising candidates for topological quantum computation [19]. A particularly intriguing platform is small-angle twisted bilayer MoTe₂, where the second moiré bands are predicted to host non-Abelian fractional Chern insulators [20–25], while experiments have uncovered an even more exotic phase—a non-Abelian fractional spin Hall insulator [13, 14]. Notably, in these flat Chern band systems, chiral superconductivity has also been experimentally observed [26], generating considerable interest in uncovering the relationship between superconductivity and topological phases [27–36].

In this manuscript, we identify another intriguing quantum state, namely an intervalley superconducting phase, that can arise in this strongly correlated topological flat band system. Specifically, we report evidence for such a phase proximate in the phase diagram to the non-Abelian fractional spin Hall insulator in the half-filled second moiré bands, i.e., hole filling $\nu_h = 3$, of approximately 2°-twisted bilayer MoTe₂ [13, 14, 37]. We perform exact diagonalization on a continuum model of the half-filled second moiré bands, incorporating both valleys

and screened Coulomb interactions [37]. Superconductivity emerges when the short-range component of the intervalley interactions is screened, yielding time-reversal symmetry and extended *s*-wave pairing.

We further propose two complementary pairing mechanisms underlying the observed superconductivity: a Kohn–Luttinger pairing instability [38] on the metallic side and anyon superconductivity [39, 40] emerging from the non-Abelian spin Hall insulator. The former originates from the screening of repulsive Coulomb interactions, which generates an effective attractive pairing channel, similar to recent studies of superconductivity in the first moiré band of twisted bilayer MoTe₂ [27, 28]. Crucially, we find that the non-uniform quantum geometry of the moiré bands plays an essential role in enabling intervalley pairing. For example, when the second moiré bands in our model are replaced by first Landau levels with uniform quantum geometry, the superconducting tendency is strongly suppressed [37]. This comparison underscores the importance of realistic band geometry in stabilizing superconductivity, in agreement with recent theoretical developments [27–36, 41, 42].

Remarkably, our numerics uncovers a continuous single transition from the fractional spin Hall insulator to the superconducting state, with spectral flows closely resembling those of the continuous transition from a bilayer fractional quantum Hall state composed of two Pfaffian copies to an exciton condensate [43, 44]. This transition is further supported by our effective field-theory

* These authors contributed equally to this work.

† gilyoungcho@kaist.ac.kr

description, where superconductivity emerges from the fractional spin Hall insulator via the condensation of non-Abelian charge- $e/2$ anyons. In this description, the transition is unconventional and lies beyond the traditional Landau–Ginzburg paradigm: it simultaneously alters the global charge-conservation symmetry and the underlying topological order. At the same time, it provides a pairing mechanism in which superconductivity arises from the condensation of charged anyons rather than a Cooper pair, a mechanism that has recently attracted significant attention [29–36, 45–48].

In summary, our results in this manuscript suggest that higher moiré bands may provide a promising platform to explore the interplay between superconductivity, strong correlations, quantum geometry, and topological orders, thereby broadening the landscape of superconductivity and fractionalization beyond previous studies [29–36, 39, 40, 45–48].

Results

The Model.

As an effective description of twisted bilayer MoTe₂, we adopt the continuum model [49]. The non-interacting Hamiltonian is decomposed into the K - and K' -valleys, $\hat{h} = \hat{h}_\uparrow \oplus \hat{h}_\downarrow$, with the K -valley Hamiltonian given by

$$\hat{h}_\uparrow = \begin{bmatrix} -\frac{(\hat{\mathbf{k}}-K_+)^2}{2m^*} + v_+(\hat{\mathbf{r}}) & \gamma^*(\hat{\mathbf{r}}) \\ \gamma(\hat{\mathbf{r}}) & -\frac{(\hat{\mathbf{k}}-K_-)^2}{2m^*} + v_-(\hat{\mathbf{r}}) \end{bmatrix}, \quad (1)$$

where $\hat{\mathbf{k}}$ denotes the electron momentum, $K_\pm = R_{\theta/2}K$ are the twisted K points of the two layers by angle θ , and $v_\pm(\mathbf{r})$ and $\gamma(\mathbf{r})$ represent the moiré potentials and inter-layer tunneling, respectively. Note that the spin and valley are locked due to the Ising spin-orbit coupling [50]. In this manuscript, we focus primarily on the system with a twist angle θ close to 2° . The K' -valley Hamiltonian is obtained as the time-reversal conjugate of Eq. (1), ensuring that the entire system is time-reversal symmetric. The explicit forms of $v_\pm(\mathbf{r})$ and $\gamma(\mathbf{r})$ are specified in [51].

We also include the following interaction in our model,

$$\hat{H} = -\hat{h} + \frac{1}{2A} \sum_{s_0, s_1 \in \{\uparrow, \downarrow\}, \mathbf{p}} V_{s_0 s_1}(\mathbf{p}) : \hat{\rho}_{-\mathbf{p}}^{s_1} \hat{\rho}_{\mathbf{p}}^{s_0} : .$$

Here, $\hat{\rho}_{\mathbf{p}}^s$ denotes the electron density operator of momentum \mathbf{p} with spin $s \in \{\uparrow, \downarrow\}$, and A is the sample area. The interaction $V_{s_0 s_1}(\mathbf{p})$ is given by

$$V_{s_0 s_1}(\mathbf{p}) = \frac{e^2}{2\epsilon} \begin{cases} \frac{1}{p} & s_0 = s_1 \\ \frac{e^{-pd}}{p} & s_0 \neq s_1 \end{cases}. \quad (2)$$

Notably, while the intravalley interaction ($s_0 = s_1$) is simply given by the Coulomb potential, the intervalley interaction ($s_0 \neq s_1$) is the screened form arising from

band mixing with an effective screening length d , as phenomenologically introduced in [37].

A few remarks are in order. First, at a twist angle near 2° , the K -valley of twisted bilayer MoTe₂ realizes a sequence of Chern bands, all with $C = +1$, closely resembling the sequential Landau levels of a conventional two-dimensional electron gas [52]. The resemblance is not limited to the band topology alone: the effective interactions within each moiré bands strikingly mirror the Haldane pseudopotentials of their corresponding Landau levels [20]. Secondly, the moiré bands possess almost ideal dispersion and geometry [20–25], such that a half-filled *single-valley* second moiré band—remarkably akin to the first Landau level—can stabilize a non-Abelian fractional Chern insulator [20–25], specifically the Pfaffian state [21]. This may be relevant to the resistivity plateau near the filling $\nu_h = 3/2$ observed in experiment [13, 14]. The band dispersion and quantum geometry of our model can be found in [51].

Phase Diagram.

We map out the phase diagram [Fig. 1(a)] of the half-filled second moiré bands, i.e., hole filling $\nu_h = 3$, as d in Eq. (2) is tuned, which hosts both ferromagnetic Chern insulators and fractional spin Hall insulators, as well as a possible intermediate phase. Notably, both ferromagnetism and fractional spin Hall insulators have already been observed experimentally in different devices at the corresponding filling near 2° twist [13, 14, 53].

To build intuition, we first examine the two limiting cases of Eq. (2), $d \rightarrow 0$ and $d \rightarrow +\infty$. In the $d \rightarrow 0$ limit, intervalley and intravalley interactions become indistinguishable, and Stoner’s mechanism drives ferromagnetism. The holes then spontaneously choose one valley to occupy, giving rise to magnetization—or equivalently, valley polarization. Because the occupied band carries a Chern number, this realizes a ferromagnetic Chern insulator. At the opposite limit, $d \rightarrow +\infty$, the valleys decouple entirely. Each half-filled moiré band, forming a time-reversal pair, stabilizes the Pfaffian state and its time-reversal conjugate, together yielding the fractional spin Hall insulator [37]. As both are gapped phases, their stability is expected to extend to finite d [Fig. 1(a)].

We employ exact diagonalization (ED) to systematically examine the stability of both phases with varying d . ED is performed with periodic boundary conditions on system sizes $N = 12, 14$, and 16 [51]. Our ED results largely confirm the intuition developed above, but also reveal an unexpected intermediate phase [Fig. 1(a)]. For example, the ground-state energies in each magnetization sector [Fig. 1(b)] show that the model stabilizes a ferromagnetic Chern insulator for $d < d_{c,1} \approx 0.15 a_M$ as expected, while it becomes paramagnetic for $d > d_{c,1}$. Similarly, we observe clear stabilization of the fractional spin Hall insulator for $d > d_{c,2} \approx 0.34 a_M$ [Fig. 1(c,d)],

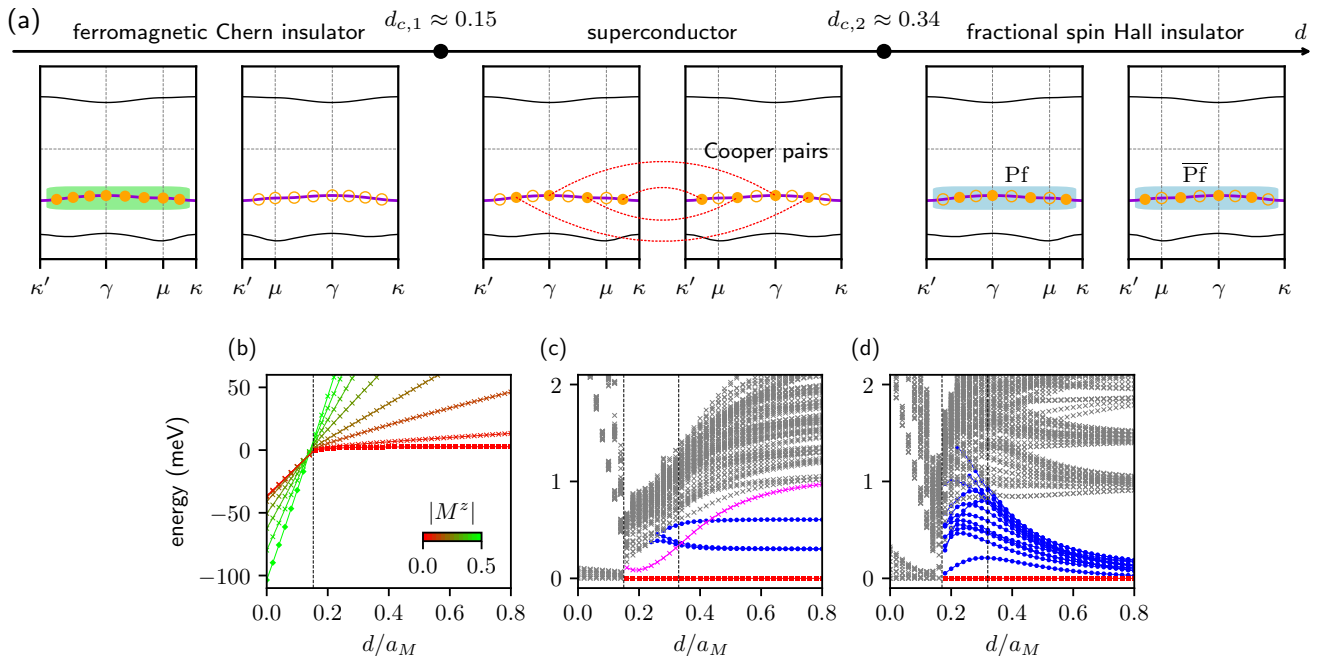


FIG. 1: **Schematic phase diagram and evolution of many-body spectrum.** (a) Schematic phase diagram as a function of d in Eq. (2), with $a_M = 1$. As d increases from 0 to $+\infty$, the system evolves through a ferromagnetic Chern insulator, a superconductor, and finally a fractional spin Hall insulator. (b) The lowest energy of each magnetization subspace for $N = 14$. (c,d) Evolution of the many-body spectrum within the paramagnetic sector $M_z = 0$ for $N = 14$ and 12 , respectively. The evolution of the many-body spectrum suggests there are two transition points, a first-order transition $d_{c,1}$ which changes the magnetization, and another continuous transition at $d_{c,2}$ which changes the nature of the ground-state manifold and excitations.

where the system shows a ground-state degeneracy of 36 for $N = 12, 16$ [51] and 4 for $N = 14$ [Fig. 2(a)], consistent with the even-odd effect expected for this phase [54]. The 4π -periodic spectral flow of the ground-states in this regime under time-reversal symmetric flux insertion, confirmed by tracking the wavefunction fidelities, further supports this [Fig. 2(b)].

Beyond the two anticipated phases, we uncover an intermediate phase, characterized by a singly-degenerate paramagnetic ground-state appearing for $d \in (d_{c,1}, d_{c,2})$ [Fig. 2(c)]. Tracking the wavefunction fidelities, we find that the other low-lying states that previously belonged to the ground-state manifold of the fractional spin Hall insulator now hybridize with excited states. Furthermore, the change in ground-state degeneracy compared to the fractional spin Hall insulator ($d > d_{c,2}$) is not merely a finite-size effect, as evidenced by the distinct evolution of the many-body spectrum under time-reversal symmetric flux insertion. Unlike the 4π -periodic spectral flow of the fractional spin Hall insulator, the unique ground-state of the intermediate phase remains isolated from excited states and exhibits a 2π -periodic spectral flow [Fig. 2(d)]. The change in many-body topology is further evidenced by the spin Hall con-

ductivity which changes from $\sigma_s = e^2/h$ for $d > d_{c,2}$ to $\sigma_s = 0$ for $d_{c,1} < d < d_{c,2}$ [51]. Finally, we also find that the ground-state energy derivatives and ground-state fidelity indicate a continuous phase transition at $d = d_{c,2}$ between the intermediate phase and the fractional spin Hall insulator [51].

Both the features and spectral flow of the ground-states closely resemble those of the continuous transition from bilayer fractional quantum Hall states of two Pfaffian copies to an exciton condensate [43, 44]. As we will show later, this continuous transition is consistent with our identification of the intermediate state as a superconducting phase. In [51], we further present data demonstrating the enhanced transition behavior when the short-range repulsion—specifically, the zeroth Haldane pseudopotential [55]—is explicitly suppressed.

In [51], we also present the many-body spectra and their evolution in the generalized first Landau level and its time-reversal conjugate with non-uniform quantum geometry. In the idealized first Landau level at $N = 14$ with uniform quantum geometry, the system appears to undergo a direct transition from the ferromagnetic Chern insulator to the fractional spin Hall insulator, with no intermediate phase showing a 1-fold degeneracy.

ate ground-state [37]. However, upon introducing non-uniform quantum geometry [56–58], the intermediate state emerges and becomes visible. This demonstrates that non-uniform quantum geometry plays a crucial role in stabilizing the intermediate phase, even without explicit band dispersion.

Intermediate Superconductivity.

We now present several pieces of evidence indicating that the intermediate state is a superconductor. Our first clue from the many-body spectrum is that the ground-state carries zero total magnetization and mo-

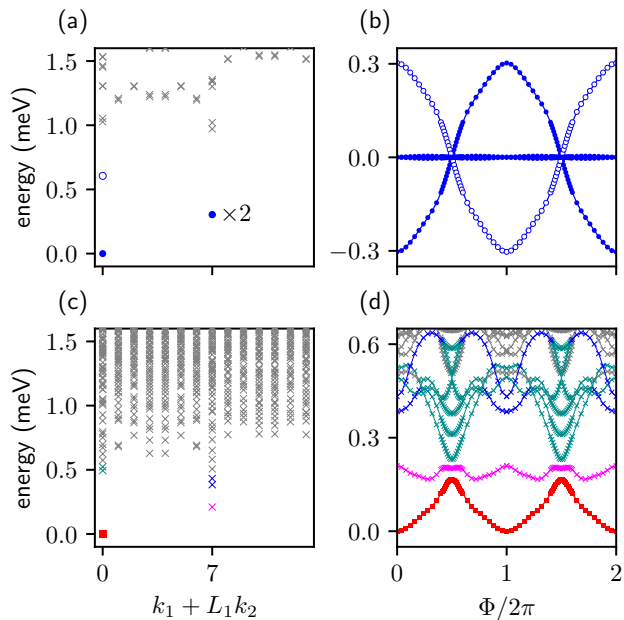


FIG. 2: **Many-body spectrum and spectral flow for $N = 14$.** (a) Many-body spectrum at $d/a_M = 0.80$ (blue circle and gray x markers). (b) Spectral flow under time-reversal symmetric flux insertion at $d/a_M = 0.80$. We find a 4π -periodic spectral flow which mixes the four lowest states (blue circles), consistent with the fractional spin Hall insulator. (c) Many-body spectrum at $d/a_M = 0.28$ (red square, magenta, blue, cyan, and gray x markers). The red square (ground-state) and two blue x markers are the wavefunctions with greatest similarity to three of the four ground-state wavefunctions of the fractional spin Hall insulator. The two cyan x markers both have large contributions from the last fractional spin Hall insulator ground-state wavefunction. The first excited state is the magenta x marked state, which is not adiabatically connected to the fractional spin Hall insulator ground-state wavefunctions. (d) Under time-reversal symmetric flux insertion of (c), the unique ground-state at $d/a_M = 0.28$ remains isolated from the excited states. The spectral flow is 2π -periodic.

mentum across all numerically-accessible system sizes and neighboring fillings in the intermediate regime $d \in (d_{c,1}, d_{c,2})$ [51]. This is consistent with Cooper pairing between holes of opposite spins and valleys at opposite momenta, i.e., between (\uparrow, \mathbf{k}) and $(\downarrow, -\mathbf{k})$. An additional signature is seen in the intervalley entanglement entropy, $S_0^{(v)} = -\text{tr}(\hat{\rho}_{0,\uparrow} \ln \hat{\rho}_{0,\uparrow})$, which changes abruptly from large values in the intermediate regime $d \in (d_{c,1}, d_{c,2})$ to small values in the fractional spin Hall insulators ($d > d_{c,2}$) [Fig. 3(a)]. Here $\hat{\rho}_{0,\uparrow}$ is the K -valley reduced density operator of the ground-state wavefunction, obtained by partially tracing out the K' -valley Hilbert space. This behavior further supports the picture of intervalley pairing, which inherently links and entangles the two valleys [Fig. 1(a)].

We further observe that the intermediate state exhibits a quantitatively enhanced tendency to form Cooper pairs, as indicated by the binding energy,

$$E_b^{(\pm)} = E_{N\pm 2,0} + E_{N,0} - 2E_{N\pm 1,0},$$

where $E_{N_h,0}$ is the ground-state energy for N_h holes. Across all three system sizes $N = 12, 14, 16$, we find that the binding energy is negative for all d , with its magnitude $|E_b|$ comparable to the Fermi energy $E_F \approx 1.50\text{meV}$ for the intermediate regime $d \in (d_{c,1}, d_{c,2})$, significantly smaller for $d > d_{c,2}$, and attaining a maximum slope at $d \approx d_{c,2}$ [Fig. 3(b)]. The identification of the intermediate state as a superconductor is further corroborated by

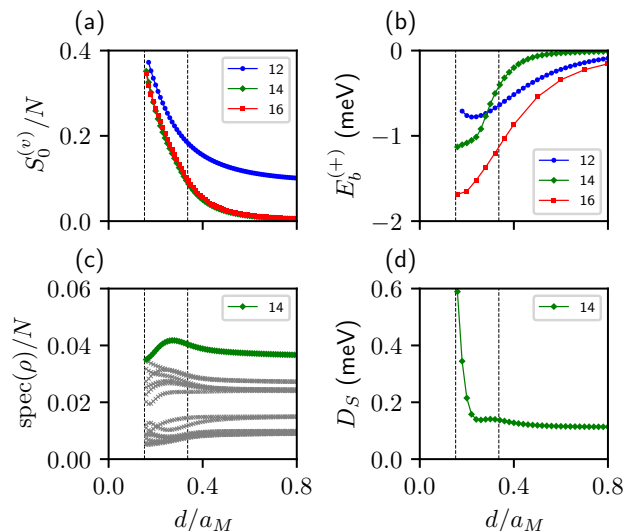


FIG. 3: **Signatures of superconductivity.** (a) Intervalley entanglement entropy $S_0^{(v)}$, (b) Binding energy $E_b^{(+)}$, (c) Spectrum of the normalized pair density matrix $\rho_{\mathbf{k}'\mathbf{k}}/N$, and (d) Superfluid stiffness D_S of the ground-state over d .

the spectrum of the pair density matrix [59],

$$\rho_{\mathbf{k}'\mathbf{k}} = \langle \hat{\Delta}_{\mathbf{k}'}^\dagger \hat{\Delta}_{\mathbf{k}} \rangle_0, \quad \hat{\Delta}_{\mathbf{k}}^\dagger = \hat{\psi}_{\uparrow,\mathbf{k}}^\dagger \hat{\psi}_{\downarrow,-\mathbf{k}}^\dagger, \quad (3)$$

where $\hat{\psi}_{s,\mathbf{k}}^\dagger$ is the operator that creates a hole in the second moiré band with spin s and crystal momentum \mathbf{k} . We observe that the pair density matrix shows a single dominant eigenvalue, well separated from the rest of the spectrum, and also this eigenvalue reaches its maximum within the intermediate regime $d \in (d_{c,1}, d_{c,2})$ [Fig. 3(c)]. Both results show a tendency for binding, specifically between (\uparrow, \mathbf{k}) and $(\downarrow, -\mathbf{k})$, which is maximized in the intermediate region. In [51], we make a similar analysis of the excitonic pair density matrix, and rule out intervalley exciton condensation as a candidate for the intermediate phase.

A defining hallmark of superconductivity is global phase coherence, captured by the superfluid stiffness D_S . We evaluate D_S from the curvature of the ground-state energy with respect to global flux insertion around the non-contractible loops of the torus [60, 61]. We find that the superfluid stiffness reaches a maximum at $d_{c,1}$ and falls to zero as d approaches $d_{c,2}$ [Fig. 3(d)]. This indicates that the intermediate region maximizes not only the pairing tendency but also phase coherence, establishing it as a superconductor.

Building on these results, we can now analyze the pairing symmetry of the superconducting state by evaluating the order parameter

$$\Delta_{\mathbf{k}} = \langle N, 0 | \hat{\psi}_{\downarrow,-\mathbf{k}} \hat{\psi}_{\uparrow,\mathbf{k}} | N + 2, 0 \rangle,$$

with $|N_h, 0\rangle$ denoting the many-body ground-state for N_h holes. The resulting wavefunction [Fig. 4(a,b)] is real, ensuring time-reversal symmetry, and its momentum-space structure belongs to the trivial irreducible representation (A_1) of the point group symmetry generated by C_3^z and $C_2^y \mathcal{T}$. The sign change across the Brillouin zone naturally classifies the superconducting state as a nodal extended s -wave superconductor. As we note in [51], the wavefunction that maximizes the pair density matrix Eq. (3) exhibits the same pairing symmetry, providing further confirmation of the result. The nodal character of the resulting superconductivity is further corroborated by the observation that the superfluid stiffness D_s is comparable to the binding energy $|E_b|$, reaching a maximum ratio of $D_s/(|E_b|/2) \approx 0.9$. This stands in contrast to conventional fully gapped superconductors, where $D_s \gg |E_b|/2$ [62, 63].

In [51], we report several additional observations. First, as expected, we observe that the many-body spectrum in our model is adiabatically connected to that of an ideal extended s -wave superconductor, realized when a strong attractive interaction in this pairing channel is introduced. In addition, we have also computed the charge gap, whose behavior is again consistent with a nodal superconductor. Finally, we find

that the binding energy and Fermi energy are of comparable magnitude and estimate a relatively short superconducting coherence length [51], placing the intermediate superconducting state in the BCS–BEC crossover regime [63], consistent with experimental observations in moiré flat band superconductors of magic-angle twisted bilayer graphene [64, 65], magic-angle twisted trilayer graphene [66, 67], and first moiré band twisted bilayer MoTe₂ [26]. We note that our estimate for superconducting coherence length incorporates quantum geometric contributions [68–72].

Kohn-Luttinger Instability.

The superconductivity observed in our exact diagonalization calculations can be understood in terms of the Kohn–Luttinger mechanism [38]. In particular, the continuum moiré band model in Eq. (1) exhibits both finite dispersion and non-uniform quantum geometry, the latter effectively contributing to dispersion effects when expressed in the hole representation [27, 51]. As detailed in [51], we find that several factors—the presence of multiple Fermi

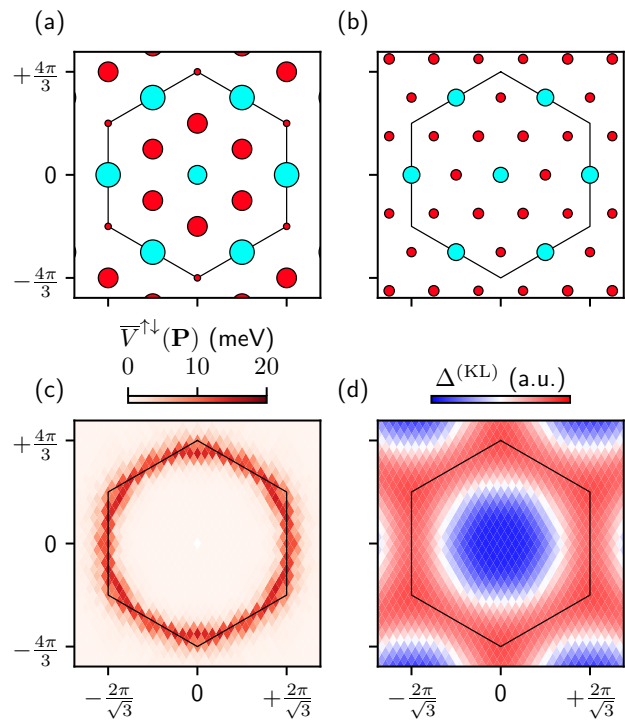


FIG. 4: **Pairing symmetry and Kohn-Luttinger instability.** (a,b) Cooper-pair order parameter for $N = 12$ and 16 , respectively. The size of the circle is proportional to the absolute value of the order parameter at the corresponding momenta, and red and cyan colors indicate opposite signs. (c) Random-phase-approximation-screened intervalley interaction. (d) Corresponding leading pairing instability. All calculations are done for $d/a_M = 0.28$.

surface pockets [73], the proximity of van Hove singularities to the Fermi surfaces [74, 75], the large quantum metric associated with the first-Landau-level-like character of the band, non-uniform quantum geometry [41], and spin anisotropy—work together to generate substantial screening of the intervalley interaction [Fig. 4(c)].

We find that, once screening within the random-phase approximation is taken into account, the interaction increases with momentum, naturally favoring a sign-changing superconducting order parameter [41]. Solving the linearized Bardeen–Cooper–Schrieffer gap equation, we identify the leading pairing instability [Fig. 4(d)] as a sign-changing extended s -wave state in the A_1 irreducible representation, consistent with the symmetry and overall structure of the gap function obtained from our exact diagonalization calculations.

Field Theory for Continuous Transition at $d_{c,2}$.

Our exact diagonalization calculations reveal a direct continuous transition from the non-Abelian fractional spin Hall insulator to an s -wave superconductor, where topological order and symmetry, i.e., charge conservation symmetry, change simultaneously. Here, by topological order we refer to the underlying anyon topological data [76–82]. In this sense, the superconducting phase corresponds to a trivial fermionic topological order [78, 79, 83], whereas the fractional spin Hall insulator realizes the $\text{Pf} \times \overline{\text{Pf}}$ topological order. Such a transition, lying beyond the traditional Landau–Ginzburg framework of symmetry breaking, warrants further theoretical explanation. We provide a field theoretic description of this continuous transition from the non-Abelian fractional spin Hall insulator to the superconductor, building on the $\text{U}(2)_{2,-4} \times \text{U}(1)_8$ Chern-Simons theory of the Pfaffian state [84–87].

Because the fractional spin Hall insulator in our model is adiabatically connected to the limit $d \rightarrow +\infty$, where the two half-filled valleys decouple and each supports a Pfaffian state [21], the resulting topological order of the fractional spin Hall insulator is $\text{Pf} \times \overline{\text{Pf}}$, with $\overline{\text{Pf}}$ denoting the time-reversal conjugate of the Pfaffian order. Its field theoretic description is

$$\begin{aligned} \mathcal{L}_{\text{Pf} \times \overline{\text{Pf}}} &= \mathcal{L}_{\text{Pf}} + \mathcal{L}_{\overline{\text{Pf}}} \\ &= -\frac{2}{4\pi} \text{Tr} \left(a da + \frac{2}{3} a^3 \right) + \frac{3}{4\pi} \text{Tr} a d \text{Tr} a + \frac{1}{2\pi} A d \text{Tr} a \\ &\quad + \frac{2}{4\pi} \text{Tr} \left(b db + \frac{2}{3} b^3 \right) - \frac{3}{4\pi} \text{Tr} b d \text{Tr} b - \frac{1}{2\pi} A d \text{Tr} b, \end{aligned}$$

where a, b are the dynamical $\text{U}(2)$ gauge fields and A is the background electromagnetic gauge field.

The superconducting phase emerges from the condensation of the bifundamental field Φ , which is coupled to the gauge fields through $D\Phi = \partial\Phi - ia\Phi - i\Phi b$. Notably, we identify the field Φ with the anyon $\sigma_{\frac{1}{4}} \otimes \sigma_{\frac{1}{4}}^T$ [51], where

$\sigma_{\frac{1}{4}}$ denotes the non-Abelian charge- $e/4$ anyon in the Pfaffian theory [30, 88] and $\sigma_{\frac{1}{4}}^T$ represents its time-reversal partner. This anyon Φ is self-bosonic, yet exhibits non-trivial braiding statistics with other anyons in the theory, e.g., $\psi_0 \otimes \sigma_{\frac{1}{4}}^T$, and possesses multiple fusion channels, i.e., it is non-Abelian [51]. To model the condensation transition, we introduce the potential

$$V(\Phi^\dagger \Phi) = m^2 \text{Tr} \Phi^\dagger \Phi + \lambda_1 \text{Tr} \Phi^\dagger \Phi \Phi^\dagger \Phi + \frac{\lambda_2}{2} (\text{Tr} \Phi^\dagger \Phi)^2,$$

with the real coefficients m^2 , λ_1 , and λ_2 . When $m^2 < 0$, the potential $V(\Phi^\dagger \Phi)$ is minimized at $\langle \Phi \rangle = sI$ with $s > 0$. This condensation enforces the constraint $\alpha \equiv a = -b$ at low energies, leading to the effective theory

$$\mathcal{L}_{\text{Pf} \times \overline{\text{Pf}}} \rightarrow \frac{2}{2\pi} A d \text{Tr} \alpha, \quad (4)$$

which is precisely the effective field theory of a superconductor [83]. Several technical field-theoretic details of the condensed phase, including the fate of the $\text{U}(2)$ gauge fields, the compactification of $\text{Tr} \alpha$, and the absence of gapless Goldstone modes associated with Φ , can be found in [51].

We conclude with a few remarks. First, transitions of this type, known as Chern–Simons–Landau–Ginzburg transitions, have been extensively studied in the literature and are widely believed to be continuous [89–102]. Our exact diagonalization results are consistent with these observations. Second, the above field-theoretic analysis indicates that the transition is driven by the condensation of the charge- $e/2$ self-bosonic non-Abelian anyon Φ , identified as the composite of $\sigma_{\frac{1}{4}}$ in Pf and its time-reversal partner $\sigma_{\frac{1}{4}}^T$ in $\overline{\text{Pf}}$. This interpretation is further reinforced by the category-theoretic framework of anyon superconductivity recently developed in [48], whose application to the present system is presented in detail in [51]. Finally, the above construction generalizes straightforwardly to the case of $\text{aPf} \times \text{a}\overline{\text{Pf}}$, with aPf denoting the anti-Pfaffian order [51].

Discussion

In this manuscript, we theoretically uncover the remarkable emergence of superconductivity from strongly correlated topological flat bands, realized as an intermediate phase between the ferromagnetic Chern insulator and the non-Abelian fractional spin Hall insulator. This superconducting state is identified through multiple hallmarks, including negative binding energy, distinctive spectral features of the pair density matrix, and finite phase stiffness. Direct evaluation of the order parameter and the dominant wavefunction of the pair density matrix reveals its pairing symmetry to be time-reversal symmetric, extended nodal s -wave. We further elucidate two complementary pairing mechanisms: a Kohn–Luttinger instability arising from non-uniform quantum geometry when

approached from the normal metallic side [27, 28, 41], and the condensation of charge- $e/2$ anyons when approached from the fractional spin Hall insulator. In particular, the latter mechanism establishes our system as a realistic platform for realizing anyon superconductivity [29–36, 39, 40, 45–48].

The experimental observation of both ferromagnetism [53] and the fractional spin Hall insulator [13, 14] in twisted bilayer MoTe_2 strongly suggests that tuning between these regimes could open a pathway to realizing the intermediate superconducting phase uncovered in our analysis. More specifically, the effective screening length d could be tuned through gating or substrate engineering, thereby promoting superconductivity. This follows from the two following observations. First, the length scale d arises from band mixing and is roughly set by the inverse of the effective band gap between the first and second moiré bands [37]. Second, in twisted bilayer MoTe_2 , the Coulomb energy is comparable to the bare band gap, so at filling $\nu_h = 3$ the effective band gap is strongly renormalized by interactions. As a result, by controlling interactions—and thereby the effective band gap—the parameter d can be effectively controlled. Indeed, a rough estimate of d for experimentally available devices [103] places it near the transition points [51], suggesting that superconductivity may be within experimental reach. Additionally, larger-scale numerical studies—such as quasi-one-dimensional density-matrix renormalization group calculations—would be valuable for further mitigating the finite-size effects inherent in our exact diagonalization results and for performing systematic scaling analyses near the anyon-condensation transition [51], thereby yielding deeper insight into the physics of this model.

Methods

Hartree-Fock Band Calculations.

Because of computational constraints, our exact diagonalization studies are limited to a single band per valley. To account for corrections from emptying the first moiré bands and to focus on the half-filled second moiré bands ($\nu_h = 3$), we performed self-consistent Hartree-Fock calculations at $\nu_h = 2$, including the four highest moiré bands. The corresponding renormalized bands and their quantum geometries are provided in the Supplementary Materials [51].

Exact Diagonalization.

We make use of spin $U_s(1)$, moiré translation to divide the many-body Fock space into subspaces of fixed hole number, magnetization, and momentum. When applicable, we also apply C_2^y , valley-reduced inversion [20, 104], and time-reversal symmetries. Within each subspace, the many-body Hamiltonian is represented with a sparse matrix, and diagonalized using Krylov methods.

We note that we estimate the superconducting coher-

ence length as $\ell_{\text{SC}} \approx 1.83 a_M$ [51], which is less than the side lengths of the finite lattices used in our calculations. As such, we expect superconducting pairing to be visible, despite finite-size effects [51].

- *Note Added:* While finalizing this manuscript, we became aware of a paper with some overlapping results [105]. In this paper, the authors tuned the intervalley interaction in a different form from Eq. (2), and also found a superconductor between the ferromagnetic Chern insulator and non-Abelian fractional spin Hall insulator at half-filling.

Acknowledgments

We thank Fiona Burnell, Debanjan Chowdhury, Hee-Cheol Kim, Yong Baek Kim, Yves Kwan, Inti Sodemann, Ashvin Vishwanath, and Ya-Hui Zhang for helpful discussions. This work is financially supported by Samsung Science and Technology Foundation under Project Number SSTF-BA2401-03, the NRF of Korea (Grants No. RS-2024-00410027, RS-2023-NR119931, RS-2024-00444725, RS-2023-00256050, RS-2025-25453111, RS-2025-08542968) funded by the Korean Government (MSIT), the Air Force Office of Scientific Research under Award No. FA23862514026, and Institute of Basic Science under project code IBS-R014-D1. This work was performed in part at Aspen Center for Physics, which is supported by National Science Foundation grant PHY-2210452. The work from DGIST was supported by the National Research Foundation of Korea (NRF) (Grant No. RS-2025-00557717, RS-2023-00269616) and the Nano and Material Technology Development Program through the National Research Foundation of Korea (NRF) funded by Ministry of Science and ICT (No. RS-2024-00444725). We also acknowledge the partner group program of the Max Planck Society. Part of this work was supported by Global Partnership Program of Leading Universities in Quantum Science and Technology (RS-2025-02317602)

Competing interests

The authors declare no competing interest.

Author Contributions

G. Y. C. conceived and supervised the project. C. A. performed the Hartree-Fock analysis, exact diagonalization calculations on moiré bands, and numerical characterization of the many-body ground-states. D. S. carried out the effective field-theory analysis and the analysis of anyon data related to anyon condensation. G. L. performed exact diagonalization calculations on generalized first Landau levels. Y. K. provided experimental inputs that informed the theoretical proposal. C. A., D. S., and G. Y. C. co-wrote the manuscript. All authors discussed the results and contributed to the final version of the manuscript.

-
- [1] Y. Cao, V. Fatemi, S. Fang, K. Watanabe, T. Taniguchi, E. Kaxiras, and P. Jarillo-Herrero, Unconventional superconductivity in magic-angle graphene superlattices, *Nature* **556**, 43 (2018).
- [2] G. Chen, A. L. Sharpe, P. Gallagher, I. T. Rosen, E. J. Fox, L. Jiang, B. Lyu, H. Li, K. Watanabe, T. Taniguchi, J. Jung, Z. Shi, D. Goldhaber-Gordon, Y. Zhang, and F. Wang, Signatures of tunable superconductivity in a trilayer graphene moiré superlattice, *Nature* **572**, 215 (2019).
- [3] Y. Cao, V. Fatemi, A. Demir, S. Fang, S. L. Tomarken, J. Y. Luo, J. D. Sanchez-Yamagishi, K. Watanabe, T. Taniguchi, E. Kaxiras, R. C. Ashoori, and P. Jarillo-Herrero, Correlated insulator behaviour at half-filling in magic-angle graphene superlattices, *Nature* **556**, 80 (2018).
- [4] E. C. Regan, D. Wang, C. Jin, M. I. Bakti Utama, B. Gao, X. Wei, S. Zhao, W. Zhao, Z. Zhang, K. Yumigeta, M. Blei, J. D. Carlström, K. Watanabe, T. Taniguchi, S. Tongay, M. Crommie, A. Zettl, and F. Wang, Mott and generalized wigner crystal states in WSe₂/WS₂ moiré superlattices, *Nature* **579**, 359 (2020).
- [5] Y. Cao, D. Chowdhury, D. Rodan-Legrain, O. Rubies-Bigorda, K. Watanabe, T. Taniguchi, T. Senthil, and P. Jarillo-Herrero, Strange metal in magic-angle graphene with near planckian dissipation, *Phys. Rev. Lett.* **124**, 076801 (2020).
- [6] F. Xu, Z. Sun, T. Jia, C. Liu, C. Xu, C. Li, Y. Gu, K. Watanabe, T. Taniguchi, B. Tong, J. Jia, Z. Shi, S. Jiang, Y. Zhang, X. Liu, and T. Li, Observation of integer and fractional quantum anomalous hall effects in twisted bilayer MoTe₂, *Phys. Rev. X* **13**, 031037 (2023).
- [7] J. Cai, E. Anderson, C. Wang, X. Zhang, X. Liu, W. Holtzmann, Y. Zhang, F. Fan, T. Taniguchi, K. Watanabe, Y. Ran, T. Cao, L. Fu, D. Xiao, W. Yao, and X. Xu, Signatures of fractional quantum anomalous hall states in twisted MoTe₂, *Nature* **622**, 63 (2023).
- [8] Y. Zeng, Z. Xia, K. Kang, J. Zhu, P. Knüppel, C. Vaswani, K. Watanabe, T. Taniguchi, K. F. Mak, and J. Shan, Thermodynamic evidence of fractional chern insulator in moiré MoTe₂, *Nature* **622**, 69 (2023).
- [9] H. Park, J. Cai, E. Anderson, Y. Zhang, J. Zhu, X. Liu, C. Wang, W. Holtzmann, C. Hu, Z. Liu, T. Taniguchi, K. Watanabe, J.-H. Chu, T. Cao, L. Fu, W. Yao, C.-Z. Chang, D. Cobden, D. Xiao, and X. Xu, Observation of fractionally quantized anomalous hall effect, *Nature* **622**, 74 (2023).
- [10] Z. Ji, H. Park, M. E. Barber, C. Hu, K. Watanabe, T. Taniguchi, J.-H. Chu, X. Xu, and Z.-X. Shen, Local probe of bulk and edge states in a fractional chern insulator, *Nature* **635**, 578 (2024).
- [11] E. Redekop, C. Zhang, H. Park, J. Cai, E. Anderson, O. Sheekey, T. Arp, G. Babikyan, S. Salters, K. Watanabe, T. Taniguchi, M. E. Huber, X. Xu, and A. F. Young, Direct magnetic imaging of fractional chern insulators in twisted MoTe₂, *Nature* **635**, 584 (2024).
- [12] H. Park, W. Li, C. Hu, C. Beach, M. Gonçalves, J. F. Mendez-Valderrama, J. Herzog-Arbeitman, T. Taniguchi, K. Watanabe, D. Cobden, L. Fu, B. A. Bernevig, N. Regnault, J.-H. Chu, D. Xiao, and X. Xu, Observation of high-temperature dissipationless fractional chern insulator (2025), [arXiv:2503.10989 \[cond-mat.mes-hall\]](https://arxiv.org/abs/2503.10989).
- [13] K. Kang, B. Shen, Y. Qiu, Y. Zeng, Z. Xia, K. Watanabe, T. Taniguchi, J. Shan, and K. F. Mak, Evidence of the fractional quantum spin hall effect in moiré MoTe₂, *Nature* **628**, 522 (2024).
- [14] K. Kang, Y. Qiu, B. Shen, K. Lee, Z. Xia, Y. Zeng, K. Watanabe, T. Taniguchi, J. Shan, and K. F. Mak, Time-reversal symmetry breaking fractional quantum spin hall insulator in moiré MoTe₂ (2025), [arXiv:2501.02525 \[cond-mat.mes-hall\]](https://arxiv.org/abs/2501.02525).
- [15] Z. Lu, T. Han, Y. Yao, A. P. Reddy, J. Yang, J. Seo, K. Watanabe, T. Taniguchi, L. Fu, and L. Ju, Fractional quantum anomalous hall effect in multilayer graphene, *Nature* **626**, 759 (2024).
- [16] Z. Lu, T. Han, Y. Yao, Z. Hadjri, J. Yang, J. Seo, L. Shi, S. Ye, K. Watanabe, T. Taniguchi, and L. Ju, Extended quantum anomalous hall states in graphene/hbn moiré superlattices, *Nature* **637**, 1090 (2025).
- [17] J. Xie, Z. Huo, X. Lu, Z. Feng, Z. Zhang, W. Wang, Q. Yang, K. Watanabe, T. Taniguchi, K. Liu, Z. Song, X. C. Xie, J. Liu, and X. Lu, Tunable fractional chern insulators in rhombohedral graphene superlattices, *Nature Materials* **24**, 1 (2025).
- [18] S. H. Aronson, T. Han, Z. Lu, Y. Yao, J. P. Butler, K. Watanabe, T. Taniguchi, L. Ju, and R. C. Ashoori, Displacement field-controlled fractional chern insulators and charge density waves in a graphene/hbn moiré superlattice, *Phys. Rev. X* **15**, 031026 (2025).
- [19] C. Nayak, S. H. Simon, A. Stern, M. Freedman, and S. Das Sarma, Non-abelian anyons and topological quantum computation, *Rev. Mod. Phys.* **80**, 1083 (2008).
- [20] C.-E. Ahn, W. Lee, K. Yananose, Y. Kim, and G. Y. Cho, Non-abelian fractional quantum anomalous hall states and first landau level physics of the second moiré band of twisted bilayer MoTe₂, *Phys. Rev. B* **110**, L161109 (2024).
- [21] A. P. Reddy, N. Paul, A. Abouelkomsan, and L. Fu, Non-abelian fractionalization in topological minibands, *Phys. Rev. Lett.* **133**, 166503 (2024).
- [22] F. Chen, W.-W. Luo, W. Zhu, and D. Sheng, Robust non-abelian even-denominator fractional chern insulator in twisted bilayer MoTe₂, *Nature Communications* **16**, 2115 (2025).
- [23] C. Xu, N. Mao, T. Zeng, and Y. Zhang, Multiple chern bands in twisted MoTe₂ and possible non-abelian states, *Phys. Rev. Lett.* **134**, 066601 (2025).
- [24] C. Wang, X.-W. Zhang, X. Liu, J. Wang, T. Cao, and D. Xiao, Higher landau-level analogs and signatures of non-abelian states in twisted bilayer MoTe₂, *Phys. Rev. Lett.* **134**, 076503 (2025).
- [25] H. Liu, Z. Liu, and E. J. Bergholtz, Non-abelian fractional chern insulators and competing states in flat moiré bands, *Phys. Rev. Lett.* **135**, 106604 (2025).
- [26] F. Xu, Z. Sun, J. Li, C. Zheng, C. Xu, J. Gao, T. Jia, K. Watanabe, T. Taniguchi, B. Tong, L. Lu, J. Jia, Z. Shi, S. Jiang, Y. Zhang, Y. Zhang, S. Lei, X. Liu, and T. Li, Signatures of unconventional superconductivity near reentrant and fractional quantum anomalous hall insulators (2025), [arXiv:2504.06972 \[cond-mat.mes-hall\]](https://arxiv.org/abs/2504.06972).

- [27] D. Guerci, A. Abouelkomsan, and L. Fu, From fractionalization to chiral topological superconductivity in a flat chern band, *Phys. Rev. Lett.* **135**, 186601 (2025).
- [28] C. Xu, N. Zou, N. Peshcherenko, A. Jahin, T. Li, S.-Z. Lin, and Y. Zhang, Chiral superconductivity from spin polarized chern band in twisted MoTe₂, *Phys. Rev. Lett.* **135**, 266005 (2025).
- [29] Z. D. Shi and T. Senthil, Doping a fractional quantum anomalous hall insulator, *Phys. Rev. X* **15**, 031069 (2025).
- [30] Z. D. Shi, C. Zhang, and S. Todadri, Doping lattice non-abelian quantum hall states, *SciPost Phys.* **19**, 150 (2025).
- [31] F. Pichler, C. Kuhlenkamp, M. Knap, and A. Vishwanath, Microscopic mechanism of anyon superconductivity emerging from fractional chern insulators, *Newton* **10.1016/j.newton.2025.100340** (2025).
- [32] T. Wang and M. P. Zaletel, *Chiral superconductivity near a fractional chern insulator* (2025), [arXiv:2507.07921 \[cond-mat.str-el\]](https://arxiv.org/abs/2507.07921).
- [33] Y.-H. Zhang, *Holon metal, charge-density-wave and chiral superconductor from doping fractional chern insulator and SU(3)₁ chiral spin liquid* (2025), [arXiv:2506.00110 \[cond-mat.str-el\]](https://arxiv.org/abs/2506.00110).
- [34] P. A. Nosov, Z. Han, and E. Khalaf, *Anyon superconductivity and plateau transitions in doped fractional quantum anomalous hall insulators* (2025), [arXiv:2506.02108 \[cond-mat.str-el\]](https://arxiv.org/abs/2506.02108).
- [35] Z. D. Shi and T. Senthil, *Anyon delocalization transitions out of a disordered fqah insulator* (2025), [arXiv:2506.02128 \[cond-mat.str-el\]](https://arxiv.org/abs/2506.02128).
- [36] Y. Huang, S. Musser, J. Zhu, Y.-Z. Chou, and S. Das Sarma, *Apparent inconsistency between streda formula and hall conductivity in reentrant integer quantum anomalous hall effect in twisted MoTe₂* (2025).
- [37] A. Abouelkomsan and L. Fu, Non-abelian spin hall insulator, *Phys. Rev. Res.* **7**, 023083 (2025).
- [38] W. Kohn and J. M. Luttinger, New mechanism for superconductivity, *Phys. Rev. Lett.* **15**, 524 (1965).
- [39] R. B. Laughlin, Superconducting ground state of non-interacting particles obeying fractional statistics, *Phys. Rev. Lett.* **60**, 2677 (1988).
- [40] R. B. Laughlin, The relationship between high-temperature superconductivity and the fractional quantum hall effect, *Science* **242**, 525 (1988).
- [41] G. Shavit and J. Alicea, Quantum geometric kohn-luttinger superconductivity, *Phys. Rev. Lett.* **134**, 176001 (2025).
- [42] A. Jahin and S.-Z. Lin, Enhanced kohn-luttinger superconductivity in geometric bands, *Phys. Rev. B* **113**, 014504 (2026).
- [43] C. Shi, S. Jolad, N. Regnault, and J. K. Jain, Phase diagram for bilayer quantum hall effect at total filling $\nu_T = 5$, *Phys. Rev. B* **77**, 155127 (2008).
- [44] Z. Zhu, S.-K. Jian, and D. N. Sheng, Exciton condensation in quantum hall bilayers at total filling $\nu_T = 5$, *Phys. Rev. B* **99**, 201108 (2019).
- [45] L. Zhang, Y.-H. Zhang, and X.-Y. Song, *Charge-4e anyon superconductor from doping SU(4)₁ chiral spin liquid* (2025), [arXiv:2508.12370 \[cond-mat.str-el\]](https://arxiv.org/abs/2508.12370).
- [46] C. Kuhlenkamp, S. Divic, M. P. Zaletel, T. Soejima, and A. Vishwanath, *Robust superconductivity upon doping chiral spin liquid and chern insulators in a hubbard-hofstadter model* (2025), [arXiv:2509.02675 \[cond-mat.str-el\]](https://arxiv.org/abs/2509.02675).
- [47] Z. D. Shi, Z. Han, S. Raghu, and A. Vishwanath, *Charge-4e superconductor with parafermionic vortices: A path to universal topological quantum computation* (2026), [arXiv:2602.06963 \[cond-mat.str-el\]](https://arxiv.org/abs/2602.06963).
- [48] D. Seo, T. Lee, and G. Y. Cho, *A unified categorical description of quantum hall hierarchy and anyon superconductivity* (2026), [arXiv:2602.03848 \[cond-mat.str-el\]](https://arxiv.org/abs/2602.03848).
- [49] F. Wu, T. Lovorn, E. Tutuc, I. Martin, and A. H. MacDonald, Topological insulators in twisted transition metal dichalcogenide homobilayers, *Phys. Rev. Lett.* **122**, 086402 (2019).
- [50] D. Xiao, G.-B. Liu, W. Feng, X. Xu, and W. Yao, Coupled spin and valley physics in monolayers of MoS₂ and other group-vi dichalcogenides, *Phys. Rev. Lett.* **108**, 196802 (2012).
- [51] (2026), see Supplemental Information at [URL].
- [52] J. Shi, N. Morales-Durán, E. Khalaf, and A. H. MacDonald, Adiabatic approximation and aharonov-casher bands in twisted homobilayer transition metal dichalcogenides, *Phys. Rev. B* **110**, 035130 (2024).
- [53] W. Li, E. Redekop, C. Wang Beach, C. Zhang, X. Zhang, X. Liu, W. Holtzmann, C. Hu, E. Anderson, H. Park, T. Taniguchi, K. Watanabe, J.-h. Chu, L. Fu, T. Cao, D. Xiao, A. F. Young, and X. Xu, Universal magnetic phases in twisted bilayer MoTe₂, *Nano Letters* **25**, 18044 (2025).
- [54] M. Oshikawa, Y. B. Kim, K. Shtengel, C. Nayak, and S. Tewari, Topological degeneracy of non-abelian states for dummies, *Annals of Physics* **322**, 1477 (2007).
- [55] Y. H. Kwan, G. Wagner, J. Yu, A. K. Dagnino, Y. Jiang, X. Xu, B. A. Bernevig, T. Neupert, and N. Regnault, Regarding the existence of abelian fractional topological insulators in twisted MoTe₂ and related systems, *Communications Physics* **9**, 10.1038/s42005-025-02483-6 (2026).
- [56] J. Wang, J. Cano, A. J. Millis, Z. Liu, and B. Yang, Exact landau level description of geometry and interaction in a flatband, *Phys. Rev. Lett.* **127**, 246403 (2021).
- [57] M. Fujimoto, D. E. Parker, J. Dong, E. Khalaf, A. Vishwanath, and P. Ledwith, Higher vortexability: Zero-field realization of higher landau levels, *Phys. Rev. Lett.* **134**, 106502 (2025).
- [58] Z. Liu, B. Mera, M. Fujimoto, T. Ozawa, and J. Wang, Theory of generalized landau levels and its implications for non-abelian states, *Phys. Rev. X* **15**, 031019 (2025).
- [59] C. N. Yang, Concept of off-diagonal long-range order and the quantum phases of liquid he and of superconductors, *Rev. Mod. Phys.* **34**, 694 (1962).
- [60] D. J. Scalapino, S. R. White, and S. Zhang, Insulator, metal, or superconductor: The criteria, *Phys. Rev. B* **47**, 7995 (1993).
- [61] R. Resta, Drude weight and superconducting weight, *Journal of Physics: Condensed Matter* **30**, 414001 (2018).
- [62] V. J. Emery and S. A. Kivelson, Importance of phase fluctuations in superconductors with small superfluid density, *Nature* **374**, 434 (1995).
- [63] Q. Chen, Z. Wang, R. Boyack, S. Yang, and K. Levin, When superconductivity crosses over: From bcs to bec, *Rev. Mod. Phys.* **96**, 025002 (2024).
- [64] M. Oh, K. P. Nuckolls, D. Wong, R. L. Lee, X. Liu, K. Watanabe, T. Taniguchi, and A. Yazdani, Evidence for unconventional superconductivity in twisted bilayer

- graphene, *Nature* **600**, 240 (2021).
- [65] H. Tian, X. Gao, Y. Zhang, S. Che, T. Xu, P. Cheung, K. Watanabe, T. Taniguchi, M. Randeria, F. Zhang, C. N. Lau, and M. W. Bockrath, Evidence for dirac flat band superconductivity enabled by quantum geometry, *Nature* **614**, 440 (2023).
- [66] J. M. Park, Y. Cao, K. Watanabe, T. Taniguchi, and P. Jarillo-Herrero, Tunable strongly coupled superconductivity in magic-angle twisted trilayer graphene, *Nature* **590**, 249 (2021).
- [67] H. Kim, Y. Choi, C. Lewandowski, A. Thomson, Y. Zhang, R. Polski, K. Watanabe, T. Taniguchi, J. Alicea, and S. Nadj-Perge, Evidence for unconventional superconductivity in twisted trilayer graphene, *Nature* **606**, 494 (2022).
- [68] M. Iskin, Extracting quantum-geometric effects from ginzburg-landau theory in a multiband hubbard model, *Phys. Rev. B* **107**, 224505 (2023).
- [69] S. A. Chen and K. T. Law, Ginzburg-landau theory of flat-band superconductors with quantum metric, *Phys. Rev. Lett.* **132**, 026002 (2024).
- [70] J.-X. Hu, S. A. Chen, and K. T. Law, Anomalous coherence length in superconductors with quantum metric, *Communications Physics* **8**, 20 (2025).
- [71] M. Iskin, Pair size and quantum geometry in a multiband hubbard model, *Phys. Rev. B* **111**, 014502 (2025).
- [72] M. Thumin and G. Bouzerar, Correlation functions and characteristic lengthscales in flat band superconductors, *SciPost Phys.* **18**, 025 (2025).
- [73] S. Maiti and A. V. Chubukov, Renormalization group flow, competing phases, and the structure of superconducting gap in multiband models of iron-based superconductors, *Phys. Rev. B* **82**, 214515 (2010).
- [74] J. González, Kohn-luttinger superconductivity in graphene, *Phys. Rev. B* **78**, 205431 (2008).
- [75] R. Nandkishore, L. S. Levitov, and A. V. Chubukov, Chiral superconductivity from repulsive interactions in doped graphene, *Nature Physics* **8**, 158 (2012).
- [76] X.-G. Wen, A theory of 2+1d bosonic topological orders, *National Science Review* **3**, 68–106 (2015).
- [77] A. Kitaev, Anyons in an exactly solved model and beyond, *Annals of Physics* **321**, 2–111 (2006).
- [78] X.-G. Wen, Colloquium: Zoo of quantum-topological phases of matter, *Rev. Mod. Phys.* **89**, 041004 (2017).
- [79] T. Lan, L. Kong, and X.-G. Wen, Theory of (2+1)-dimensional fermionic topological orders and fermionic/bosonic topological orders with symmetries, *Phys. Rev. B* **94**, 155113 (2016).
- [80] T. Lan, L. Kong, and X.-G. Wen, Classification of (2+1)-dimensional topological order and symmetry-protected topological order for bosonic and fermionic systems with on-site symmetries, *Phys. Rev. B* **95**, 235140 (2017).
- [81] M. Barkeshli, P. Bonderson, M. Cheng, and Z. Wang, Symmetry fractionalization, defects, and gauging of topological phases, *Phys. Rev. B* **100**, 115147 (2019).
- [82] G. Y. Cho, H.-C. Kim, D. Seo, and M. You, Classification of fermionic topological orders from congruence representations, *Phys. Rev. B* **108**, 115103 (2023).
- [83] T. H. Hansson, V. Oganessian, and S. L. Sondhi, Superconductors are topologically ordered, *Annals of Physics* **313**, 497–538 (2004).
- [84] E. Fradkin, C. Nayak, A. Tsvelik, and F. Wilczek, A chern-simons effective field theory for the pfaffian quantum hall state, *Nuclear Physics B* **516**, 704 (1998).
- [85] N. Seiberg and E. Witten, Gapped boundary phases of topological insulators via weak coupling, *Prog. Theor. Exp. Phys.* **2016**, 12C101 (2016).
- [86] B. Lian and J. Wang, Theory of the disordered $\nu = \frac{5}{2}$ quantum thermal hall state: Emergent symmetry and phase diagram, *Phys. Rev. B* **97**, 165124 (2018).
- [87] P.-S. Hsin, Y.-H. Lin, N. M. Paquette, and J. Wang, Effective field theory for fractional quantum hall systems near $\nu = 5/2$, *Phys. Rev. Res.* **2**, 043242 (2020).
- [88] P. Bruillard, C. Galindo, T. Hagge, S.-H. Ng, J. Y. Plavnik, E. C. Rowell, and Z. Wang, Fermionic modular categories and the 16-fold way, *Journal of Mathematical Physics* **58**, 041704 (2017).
- [89] X.-G. Wen and Y.-S. Wu, Transitions between the quantum hall states and insulators induced by periodic potentials, *Phys. Rev. Lett.* **70**, 1501 (1993).
- [90] S.-P. Kou, J. Yu, and X.-G. Wen, Mutual chern-simons landau-ginzburg theory for continuous quantum phase transition of \mathbb{Z}_2 topological order, *Phys. Rev. B* **80**, 125101 (2009).
- [91] M. Barkeshli and X.-G. Wen, Anyon condensation and continuous topological phase transitions in non-abelian fractional quantum hall states, *Phys. Rev. Lett.* **105**, 216804 (2010).
- [92] M. Barkeshli and J. McGreevy, Continuous transition between fractional quantum hall and superfluid states, *Phys. Rev. B* **89**, 235116 (2014).
- [93] S. Gazit, F. F. Assaad, S. Sachdev, A. Vishwanath, and C. Wang, Confinement transition of \mathbb{Z}_2 gauge theories coupled to massless fermions: Emergent quantum chromodynamics and SO(5) symmetry, *Proceedings of the National Academy of Sciences* **115**, E6987 (2018).
- [94] T.-S. Zeng, D. N. Sheng, and W. Zhu, Continuous phase transition between bosonic integer quantum hall liquid and a trivial insulator: Evidence for deconfined quantum criticality, *Phys. Rev. B* **101**, 035138 (2020).
- [95] Y.-H. Wu, H.-H. Tu, and M. Cheng, Continuous phase transitions between fractional quantum hall states and symmetry-protected topological states, *Phys. Rev. Lett.* **131**, 256502 (2023).
- [96] M. Schuler, L.-P. Henry, Y.-M. Lu, and A. M. Läuchli, Emergent xy* transition driven by symmetry fractionalization and anyon condensation, *SciPost Phys.* **14**, 001 (2023).
- [97] K. Hwang, Anyon condensation and confinement transition in a kitaev spin liquid bilayer, *Phys. Rev. B* **109**, 134412 (2024).
- [98] Z. Han, T. Wang, Z. Dong, M. P. Zaletel, and A. Vishwanath, Anyon superfluidity of excitons in quantum hall bilayers (2025), [arXiv:2508.14894 \[cond-mat.str-el\]](https://arxiv.org/abs/2508.14894).
- [99] Z. Zhou, C. Wang, and Y.-C. He, Chern-simons-matter conformal field theory on fuzzy sphere: Confinement transition of kalmeyer-laughlin chiral spin liquid (2025), [arXiv:2507.19580 \[cond-mat.str-el\]](https://arxiv.org/abs/2507.19580).
- [100] K.-W. Huang, X.-J. Hou, and Y.-H. Wu, Third-order quantum phase transitions of bosonic non-abelian fractional quantum hall states (2025), [arXiv:2509.17113 \[cond-mat.str-el\]](https://arxiv.org/abs/2509.17113).
- [101] T. Wang, X.-Y. Song, M. P. Zaletel, and T. Senthil, Emergent qed₃ at the bosonic laughlin state to superfluid transition (2026), [arXiv:2507.07611 \[cond-mat.str-el\]](https://arxiv.org/abs/2507.07611).

- [102] W. Ji, R. A. Lanzetta, Z. Zhou, and C. Wang, **Self-dual higgs transitions: Toric code and beyond** (2026), [arXiv:2601.20945 \[cond-mat.str-el\]](#).
- [103] X.-W. Zhang, C. Wang, X. Liu, Y. Fan, T. Cao, and D. Xiao, Polarization-driven band topology evolution in twisted MoTe_2 and WSe_2 , **Nature Communications** **15**, 4223 (2024).
- [104] Y. Jia, J. Yu, J. Liu, J. Herzog-Arbeitman, Z. Qi, H. Pi, N. Regnault, H. Weng, B. A. Bernevig, and Q. Wu, Moiré fractional chern insulators. i. first-principles calculations and continuum models of twisted bilayer MoTe_2 , **Phys. Rev. B** **109**, 205121 (2024).
- [105] S. Das, G. Wagner, and T. Neupert, **Fractional topological insulators at odd-integer filling: Phase diagram of two-valley quantum hall model** (2025), [arXiv:2509.16335 \[cond-mat.str-el\]](#).

Supplementary Information for “Superconductivity Proximate to Non-Abelian Fractional Spin Hall Insulator in Twisted Bilayer MoTe₂”

Cheong-Eung Ahn,^{1,*} Donghae Seo,^{1,*} Gyeoul Lee,² Youngwook Kim,³ and Gil Young Cho^{4,5,†}

¹Department of Physics, Pohang University of Science and Technology, Pohang, 37673, Republic of Korea

²Department of Physics, Ulsan National Institute of Science and Technology, Ulsan 44919, Republic of Korea

³Department of Physics and Chemistry, Daegu Gyeongbuk Institute of Science and Technology (DGIST), Daegu 42988, Republic of Korea

⁴Department of Physics, Korea Advanced Institute of Science and Technology, Daejeon 34141, Republic of Korea

⁵Center for Artificial Low Dimensional Electronic Systems, Institute for Basic Science, Pohang 37673, Korea

CONTENTS

I. Additional Details on the Model	1
II. Additional Numerical Results	4
A. Additional Many-Body Spectra	4
B. Additional Signatures of the FSHI-SC Transition	5
C. Extended Phase Space with Subtracted $V_0^{(1)}$	6
D. Additional Signatures of Superconductivity	6
E. Additional Evidence of Superconducting Pairing Symmetry	8
F. BCS vs. BEC	8
III. Intermediate Superconductivity in Generalized First Landau Levels	9
IV. Kohn-Luttinger Mechanism for the Intermediate Superconductor	10
V. Field-Theoretical Description of the FSHI-SC Transition	11
VI. Categorical Description of the FSHI-SC Transition	13
VII. Superconductivity from Different non-Abelian FSHIs	14
References	15

I. ADDITIONAL DETAILS ON THE MODEL

a. Lattice Geometry We denote the moiré Brillouin zone as BZ and the moiré reciprocal lattice as $\hat{\Lambda}$. See [Fig. S1] for orientation and our choice of reciprocal lattice vectors, \mathbf{Q}_1 and \mathbf{Q}_2 .

b. Continuum Model of Twisted Bilayer MoTe₂ Let us discuss the parameters used in our paper. We used the normalization convention of setting the moiré lattice constant as unity, $a_M = a_0 (2 \sin \frac{\theta}{2})^{-1} = 1$, where $a_0 = 3.52 \text{ \AA}$ is the monolayer lattice constant and $\theta = 2.1^\circ$ is the twist angle. For the continuum model, we use the

effective mass $m^*/m_e = 0.62$, and consider the moiré potential up to valley-reduced-inversion symmetric second-harmonics [1, 2],

$$v_\ell(\mathbf{r}) = 2v_1 \sum_{j=0}^2 \cos(\mathbf{Q}_j \cdot \mathbf{r} + \ell\psi) + 2v_2 \sum_{j=0}^2 \cos(\mathbf{Q}_j^{(2)} \cdot \mathbf{r}),$$

$$\gamma(\mathbf{r}) = \gamma_1 (1 + e^{+i\mathbf{Q}_2 \cdot \mathbf{r}} + e^{-i\mathbf{Q}_1 \cdot \mathbf{r}}) + \gamma_2 (e^{-i\mathbf{Q}_0 \cdot \mathbf{r}} + e^{-i\mathbf{Q}_0^{(2)} \cdot \mathbf{r}} + e^{+i\mathbf{Q}_0 \cdot \mathbf{r}}),$$

for some real parameters $v_1, v_2, \psi, \gamma_1, \gamma_2$. The moiré reciprocal lattice vectors \mathbf{Q}_j and $\mathbf{Q}_j^{(2)}$ are as defined in [Fig. S1].

A summary of continuum model parameter values for

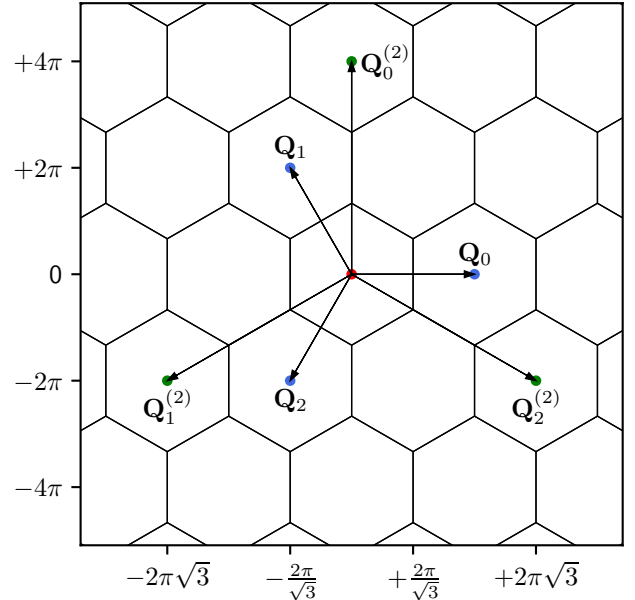


FIG. S1: **Moiré Brillouin Zone and Reciprocal Lattice.** The reciprocal lattice is generated by \mathbf{Q}_1 and \mathbf{Q}_2 . We also label $\mathbf{Q}_0 = -\mathbf{Q}_1 - \mathbf{Q}_2$ and $\mathbf{Q}_j^{(2)} = \mathbf{Q}_{j+1} - \mathbf{Q}_{j+2}$ ($j \in \mathbb{Z}/3\mathbb{Z}$).

v_1	ψ	v_2	γ_1	γ_2	Ref.
20.51	-61.49°	-9.08	-7.01	11.08	[2, 3]
17.5	-58.49°	-10.5	-6.5	11.75	[4]
2.4	-90.0°	1.0	-5.8	2.8	[5]
27.45	-58.69°	-6.50	-12.06	18.64	this paper
27.71	-59.08°	-6.44	-12.02	18.55	[Fig. S4(b)] only

TABLE S1: **Continuum model parameters for the 2MB at $\theta \sim 2^\circ$.** The parameters $v_1, v_2, \gamma_1, \gamma_2$ are in meV units.

the second moiré band (2MB) at $\theta \sim 2^\circ$ are listed in [Table S1]. For our paper, we use parameters, which have been optimized to better stabilize the non-Abelian fractional spin Hall insulator at $\theta = 2.1^\circ$. We note that while all parameter sets do stabilize the fractional quantum anomalous Hall insulator in a single valley at larger system sizes, and thus are also likely to stabilize the fractional spin Hall insulator in the thermodynamic limit, it is obscured by finite size effects for the system sizes we consider, requiring the more optimized parameters.

We denote the moiré bands with (s, ν, \mathbf{k}) , where $s \in \{\uparrow, \downarrow\}$ is the spin, ν is the band index, and $\mathbf{k} \in \text{BZ}$ is the moiré crystal momentum. That is,

$$\hat{h} |s, \nu, \mathbf{k}\rangle = \epsilon_{\mathbf{k}}^{s, \nu} |s, \nu, \mathbf{k}\rangle,$$

where $\epsilon_{\mathbf{k}}^{s, \nu}$ are the moiré band energies and $|s, \nu, \mathbf{k}\rangle$ are the corresponding single-electron states. We perform a particle-hole transformation and henceforth work with hole operators.

c. Interacting Hamiltonian Let us rewrite the interacting Hamiltonian in the moiré band basis. The many-body Hamiltonian can be written as

$$H = \sum_{s, \nu, \mathbf{k}} \epsilon_{\mathbf{k}}^{s, \nu} \psi_{\mathbf{k}}^{s, \nu \dagger} \psi_{\mathbf{k}}^{s, \nu} + \frac{1}{2A} \sum_{\substack{s_0, s_1, \\ \nu_0, \nu_1, \nu'_0, \nu'_1, \\ \mathbf{k}_0, \mathbf{k}_1, \mathbf{p}}} \mathfrak{V}_{\mathbf{k}_0 \mathbf{k}_1 \mathbf{p}}^{s_0 s_1, \nu'_0 \nu'_1 \nu_0, \nu_1} \psi_{\{\mathbf{k}_0 + \mathbf{p}\}}^{s_0, \nu'_0 \dagger} \psi_{\{\mathbf{k}_1 - \mathbf{p}\}}^{s_1, \nu'_1 \dagger} \psi_{\mathbf{k}_1}^{s_1, \nu_1} \psi_{\mathbf{k}_0}^{s_0, \nu_0},$$

where $\psi_{\mathbf{k}}^{s, \nu \dagger}$ are creation operators for the moiré band states $|s, \nu, \mathbf{k}\rangle$, and $\mathfrak{V}_{\mathbf{k}_0 \mathbf{k}_1 \mathbf{p}}^{s_0 s_1, \nu'_0 \nu'_1 \nu_0, \nu_1}$ is the two-body interaction matrix,

$$\begin{aligned} \mathfrak{V}_{\mathbf{k}_0 \mathbf{k}_1 \mathbf{p}}^{s_0 s_1, \nu'_0 \nu'_1 \nu_0, \nu_1} & \\ = \sum_{\mathbf{Q} \in \hat{\Lambda}} V^{s_0 s_1}(\mathbf{p} + \mathbf{Q}) \mathfrak{f}_{\mathbf{k}_0, \mathbf{p} + \mathbf{Q}}^{s_0, \nu'_0 \nu_0} \bar{\mathfrak{f}}_{\{\mathbf{k}_1 - \mathbf{p}\}, \mathbf{p} + \mathbf{Q}}^{s_1, \nu'_1 \nu_1}, \end{aligned} \quad (\text{S1})$$

where $V^{s_0 s_1}(\mathbf{P})$ is specified in the main text, and $\mathfrak{f}_{\mathbf{k}, \mathbf{P}}^{s, \nu' \nu}$ is the form factor,

$$\mathfrak{f}_{\mathbf{k}, \mathbf{P}}^{s, \nu' \nu} = \langle s, \nu', \{\mathbf{k} + \mathbf{P}\} | e^{+i\mathbf{P} \cdot \hat{\mathbf{r}}} | s, \nu, \mathbf{k} \rangle.$$

Here, $\{\bullet\}$ denotes the crystal momentum part of momentum, i.e. momentum modulo reciprocal lattice momentum, for some consistent prescription of the Brillouin zone, BZ, embedded in $\mathbb{R}^2 = \text{BZ} \oplus \hat{\Lambda}$.

For our paper, we use $\epsilon_r = 5$, which gives an interaction strength scale of $e^2/4\pi\epsilon a_M \approx 29.99$ meV.

d. Hartree-Fock Renormalized Second Moiré Bands In [Fig. S2], we show the Hartree-Fock renormalized second moiré bands at $\nu_h = 2$ used as the background for our many-body calculations, taking $d/a_M = 0.28$ as a representative example. The second moiré bands are very flat, with a bandwidth $\delta_{\text{HF}, 2} = 2.80$ meV $\ll e^2/4\pi\epsilon a_M$, and fairly uniform Berry curvature and trace of Fubini-Study metric, satisfying $\frac{1}{2\pi} \int_{\text{BZ}} d^2\mathbf{k} \text{tr} g_{\mathbf{k}} = 3.02$, close to the ideal value of 3 for the first Landau level.

While flat relative to the interaction scale, let us still consider the $\nu_h = 3$ Fermi surface. When considering the Fermi surface at $\nu_h = 3$, rather than considering the second moiré bands at $\nu_h = 2$, we can also equally consider the particle-hole transformed second moiré band at $\nu_h = 4$. Note that as we only perform second moiré band projected calculations, here we refer to the particle-hole transformation of the isolated $\nu_h = 2$ renormalized second moiré band, not the full Hartree-Fock renormalization for $\nu_h = 4$. In addition to being more dispersive, the

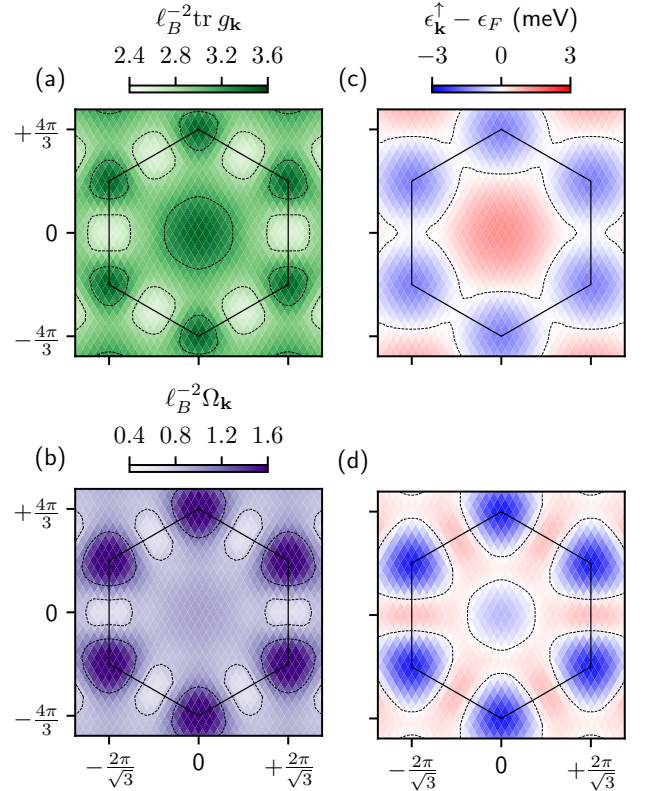


FIG. S2: **Hartree-Fock Renormalized Second Moiré Band at $d/a_M = 0.28$.** (a) Trace of Fubini-Study metric in units of l_B^{-2} . (b) Berry curvature in units of l_B^{-2} . (c) Band energies of the second moiré band relative to the Fermi energy at half-filling, together with the Fermi surface. (d) Equivalent of (c) for the particle-hole transformed electron band.

$\nu_h = 4$ band splits the Fermi surface into three γ - and κ -point centered surfaces.

We note the presence of van Hove singularities at the μ points, which are close to the $\nu_h = 3$ Fermi surface for both cases, and change occupancy across the particle-hole transformation. As such, we can expect the μ points to be relevant for near-Fermi surface physics.

e. Estimation of d Following [6], we obtained estimates for d by comparing the largest magnitudes of the intervalley and intravalley two-particle spectra. For the purposes of estimating d , we approximate the twisted bilayer MoTe₂ system with Landau levels and its' time-reversal conjugate. Comparing the ratios for the phenomenological interaction and band mixing considered up to second-order perturbations, we have the relation,

$$\begin{aligned} & \frac{1 - \frac{\pi}{2^{1/2} \cdot 3^{5/4}} \kappa}{1 - \frac{\pi}{3^{5/4} \cdot 5} \kappa} \\ &= \left(1 + \frac{2}{3} \frac{d^2}{\ell_B^2} + \frac{1}{3} \frac{d^4}{\ell_B^4} \right) e^{d^2/2\ell_B^2} \operatorname{erfc} \left(\frac{d}{\sqrt{2}\ell_B} \right) \\ & \quad - \frac{2}{3\sqrt{2}\pi} \left(\frac{d}{\ell_B} + \frac{d^3}{\ell_B^3} \right), \end{aligned}$$

where $\kappa = (e^2/4\pi a_M)/\Delta$ is the Coulomb interaction strength relative to the band gap, and ℓ_B is the effective magnetic length, $\ell_B = \sqrt{\sqrt{3}/4\pi} a_M \approx (0.37) a_M$.

When using the DFT bands at $\nu_h = 0$ [3], the gap between the moiré bands is only $\Delta_{\text{NI}} \approx 10$ meV, which corresponds to $\delta \approx 3.0$. This clearly exceeds the limits of second-order perturbation theory, with the left-hand side taking on a negative value, which cannot be attained even at $d \rightarrow \infty$. When accounting for Hartree-Fock renormalization, the effective band gap is enhanced, giving approximately $\Delta_{\text{HF}} = 20$ meV or 50 meV, depending on whether we set the background at $\nu_h = 2$ or $\nu_h = 4$. We can expect the effective band gap at $\nu_h = 3$ to be somewhere between these two values, giving us the estimate range $\kappa \in (0.6, 1.5)$. Substituting into the ratio equation, we have $d/a_M \in (0.13, 1.7)$, which includes our estimates for $d_{c,1}$ and $d_{c,2}$ in the possible range. We note that while Hartree-Fock renormalization tends to overestimate band gaps in renormalized bands, we can still expect d to be close to the transitional values identified in our main text.

f. Estimation of Superconducting Coherence Length Here, we estimate the superconducting coherence length at $d/a_M = 0.28$.

First, we consider the conventional BCS contribution arising from the band dispersion relative to the pairing gap along the Fermi surface, $\ell_{\text{BCS}} = \hbar v_F/\Delta$, which requires estimates of both the Fermi velocity and the pairing gap. When using the hole bands, native to our calculations, the average Fermi velocity is $\hbar v_F = (0.67(25) \text{ meV}) a_M$ [Fig. S2(c)]. Due to the non-uniform quantum geometry, the second moiré band is not particle-hole symmetric and the particle-hole transformed band

has a larger Fermi velocity, $\hbar v_F = (1.21(33) \text{ meV}) a_M$ [Fig. S2(d)]. We use the latter for the estimate for the superconducting coherence length. In lieu of the pairing gap, we use half of the binding energy, which for $N = 16$ is found to be $|E_b| = 1.37$ meV. Thus, we have our estimate for the conventional BCS superconducting coherence length, $\ell_{\text{BCS}} = 1.77(48) a_M$.

Second, as we are considering bands with non-trivial quantum geometry, there are also quantum geometric contributions to the superconducting coherence length [7–11], ℓ_{QM} , which combine with the conventional BCS contribution to give the complete mean-field superconducting coherence length [9],

$$\ell_{\text{SC}}^{(\text{MF})} = \sqrt{\ell_{\text{BCS}}^2 + \ell_{\text{QM}}^2}.$$

To obtain an approximate estimate of the contribution arising from the quantum geometry, we model the second moiré band by the first Landau level [2]. Within this framework, the quantum geometric contribution is given by $\ell_{\text{QM}} \approx (\det g_{\text{1LL}})^{1/4} = \sqrt{\frac{3}{2}} \ell_B = \sqrt{\frac{3\sqrt{3}}{8\pi}} a_M \approx 0.45 a_M$ where g_{1LL} is the Fubini-Study metric of the first Landau level, and ℓ_B denotes the effective magnetic length.

Combining the two contributions [9], the resulting mean-field estimate for the superconducting coherence length is given by $\ell_{\text{SC}}^{(\text{MF})} = 1.83(46) a_M$, which is dominated by the conventional BCS contribution.

We note that as a mean-field estimate, this does not incorporate the effects of interaction, despite being the dominant energy scale. In fact, as mentioned in the main text and elaborated later in Section II.F, the superconductivity we observe is likely in the BCS-BEC crossover regime so cannot be purely described at the mean field level. While we do not carry out independent estimates incorporating interactions due to the limitations inherent to our methodology, we note that numerical studies which have studied the BCS-BEC crossover with quantum geometry effects noted a suppression of the superconducting coherence length with increasing interaction strength, which is typical of the crossover regardless of quantum geometry effects [12], but interestingly, that the coherence length remains bounded below by $\sim \ell_{\text{QM}}$, even as we approach the BEC limit [10, 11], albeit with some debate on conventions for the coherence length in the strongly-correlated limit. As such, we expect our true effective coherence length to lie somewhere along the interval $\ell_{\text{SC}} \in (\ell_{\text{QM}}, \ell_{\text{SC}}^{(\text{MF})}) = (0.45, 1.83(46)) a_M$.

g. Finite Lattices and Finite-Size Effects For our exact diagonalization (ED) calculations, we used finite size periodic lattices of system sizes $N = 12, 14, 16$ [Fig. S3]. The total real space area is given by $A = (\sqrt{3}/2) a_M^2 N$. Comparing the area to the superconducting coherence length,

$$\frac{A}{\ell_{\text{SC}}^2} \gtrsim \frac{6\sqrt{3}}{(1.83(46))^2} \gtrsim 1.98,$$

even at the lowest estimate. Furthermore, the shortest periodic length in each configuration is $L_{\min}/a_M = 2\sqrt{3}, 2\sqrt{3}, 4$, which nearly doubles $\ell_{\text{SC}}^{(\text{MF})}$. As such, we can reasonably expect pairing to develop in our ED calculations, albeit subject to finite size effects.

We make note of some additional features of our finite lattices which may contribute to the generalizability of our results to the thermodynamic limit. First, while the continuum Brillouin zone in the thermodynamic limit is C_3^z symmetric, only $N = 12$ and 16 are prescribed to be C_3^z symmetric. This is why we have excluded $N = 14$ for expressing pairing symmetry, and we can expect this to have a slight impact on finite-size calculations.

Additionally, the points with the greatest differences in band energy are the γ and κ points [Fig. S2(c)], and these, together with the μ points, are also the points with the greatest discrepancies in quantum geometry from the first Landau level [Fig. S2(a,b)]. As such, which finite lattices manage to incorporate these points also have an impact on finite-size calculations. Notably, as we go from $N = 12, 14, 16$, the difference between the minimum and maximum band energy for the allowed momentum points decreases. This competes with the conventional assumptions of finite size scaling where increasing N should occur with fixed or increasing effective bandwidth, and may

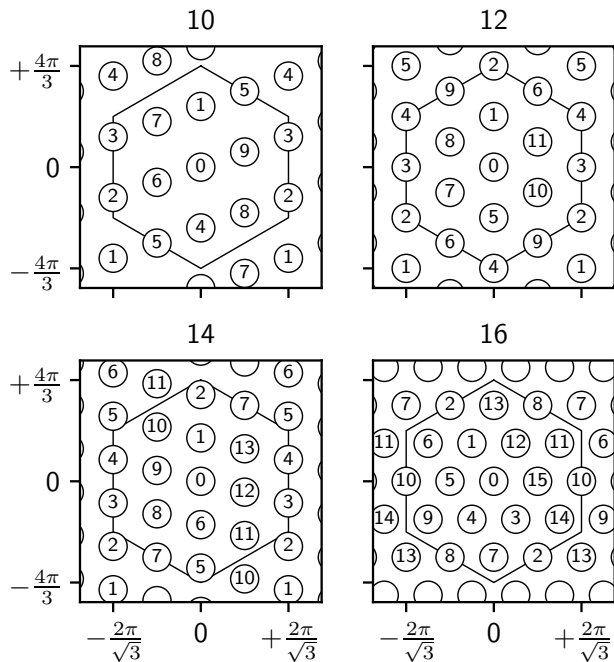


FIG. S3: **Brillouin Zone of Finite Size Triangular Lattices.** The hexagon in the background is the continuum Brillouin zone corresponding to an infinite triangular lattice. The numbered circles are the allowed crystal momenta of a discrete Brillouin zone corresponding to the finite size triangular lattice of sizes $N = 10, 12, 14, 16$.

contribute towards non-monotonic trends in our behavior over N .

Finally, we note that another complication in finite-size scaling may be the even-odd effect of the fractional spin Hall insulator (FSHI). As a general trend in our calculations, we observe that $N = 16$ shows similar behavior to $N = 12$, which is distinct from $N = 14$, with the latter typically exhibiting a sharper transition, e.g. sharper slopes, stronger peaks. Due to the different ground state degeneracy, the many-body interactions must manifest in the microscopic level repulsion statistics in distinct ways for even and odd cases, which may create distinct scaling behaviors.

In summary, while we estimate that our ED calculations to be sufficient to ascertain the existence of superconductivity and make an overall assessment of its' properties, larger scale numerical calculations will be highly valuable to obtain a more accurate understanding of the transition in the thermodynamic limit.

II. ADDITIONAL NUMERICAL RESULTS

A. Additional Many-Body Spectra

In the main text, we presented many-body spectra for the FSHI and superconductor for $N = 14$ [Fig. 2(a,c)]. In this subsection, we present representative many-body

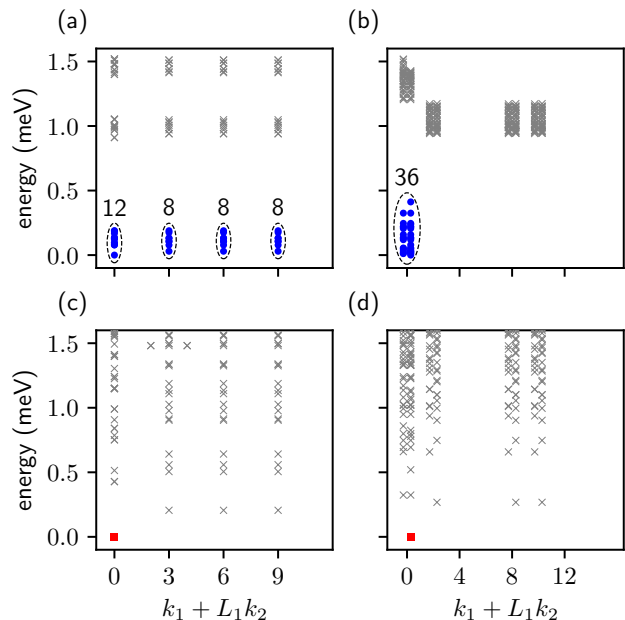


FIG. S4: **Many Body Spectrum for $N = 12$ and 16 .** (a,b) Many-body spectra for $d/a_M = 0.80$, $N = 12$ and 16 , respectively. (c,d) Many-body spectrum for $d/a_M = 0.28$, $N = 12$ and 16 , respectively. The horizontal splits for (b,d) represent charges with respect to additional symmetries used in our computations.

spectra for $N = 12$ and 16 . For $d/a_M = 0.80$, we observe 36-fold ground state degeneracy in both $N = 12$ and 16 [Fig. S4(a,b)], opposed to the 4-fold ground state degeneracy for $N = 14$, consistent with the even-odd effect expected for the FSHI [13]. Because all 36 ground states are at $\mathbf{K} = 0$ for (b), they are more strongly affected by finite-size effects, and required further optimized parameters to stabilize the FSHI [Table. S1]. For $d/a_M = 0.28$, we observe 1-fold ground state degeneracy in both $N = 12$ and 16 [Fig. S4(c,d)], same as $N = 14$.

B. Additional Signatures of the FSHI-SC Transition

In the main text, as evidence of the FSHI-SC transition, we focused on the FSHI ground state manifold, tracking its' ground state degeneracy and periodicity of spectral flow. In this subsection, we further quantify the evolution of many-body topology by computing the many-body spin Hall conductivity. We also provide independent and direct numerical evidence of the FSHI-SC transition by looking at the ground state energy and wavefunction fidelity susceptibilities.

a. Many-Body Spin Hall Conductivity We computed the many-body spin Hall conductivity from the response of the ground state wavefunction with respect to the flux insertion,

$$\sigma_{\text{sH}} = \frac{e^2}{h} C_s, \quad C_s = \frac{1}{2\pi \text{GSD}} \int_{\mathbb{T}_\theta^2} d^2\theta \text{tr} \Omega_\theta^{(s)},$$

where GSD is the ground state degeneracy, $2\pi\theta_i = \Phi_i/\Phi_0$ is the normalized flux, $\Phi_0 = h/e$ is the flux quanta, and $\Omega_\theta^{(s)}$ is the many-body Berry curvature of the ground state manifold over flux, which we have computed using a 25×25 grid. Note that the flux is coupled oppositely for opposite spins to give opposing current responses. If the single lowest energy state is isolated from the other states, which we judge by checking that the wavefunction fidelity

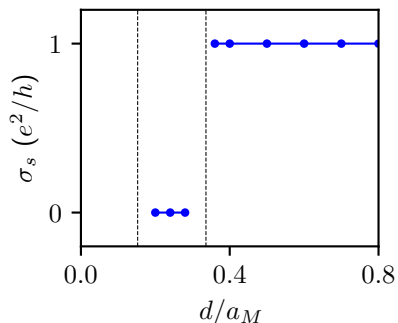


FIG. S5: **Many-Body Spin Hall Conductivity.** Computed for $N = 14$. Dashed lines are estimated transition points from ground state energy and wavefunction fidelity susceptibilities.

for all of the links across the grid are maintained above 0.75, we use the single lowest energy state with GSD = 1. If it requires mixing with the next highest state, we used GSD = 2. If non-trivial mixing with even higher states is required, we have excluded it from calculations. This was the case for $d/a_M = 0.16$ and 0.32 , which we can associate with transition points. As noted in the main text, we observe a crossover from a many-body spin Hall conductivity of $\sigma_{\text{sH}} = e^2/h$ for $d > d_{c,2}$, consistent with the FSHI, to $\sigma_{\text{sH}} = 0$ for $d < d_{c,2}$, consistent with a topologically trivial superconductor [Fig. S5].

b. Ground State Energy and Wavefunction Fidelity Susceptibilities To identify possible transitions, we wish to consider the ground state energy and wavefunction susceptibilities,

$$\chi_E^{(u)} = \frac{\partial^2 E_{\text{GS}}}{\partial u^2},$$

and

$$\chi_F^{(u)} = \lim_{\delta u \rightarrow 0^+} \frac{1 - |\langle \text{GS}; u - (\delta u/2) | \text{GS}; u + (\delta u/2) \rangle|^2}{(\delta u)^2},$$

where $E_{\text{GS}}(u)$ is the ground state energy as a function of u , $|\text{GS}; u\rangle$ is the ground state wavefunction as a function of u , and $u(d)$ is the unknown scaling field.

As we lack the system sizes to perform systematic finite size scaling, and locally determine $u(d)$, we first work

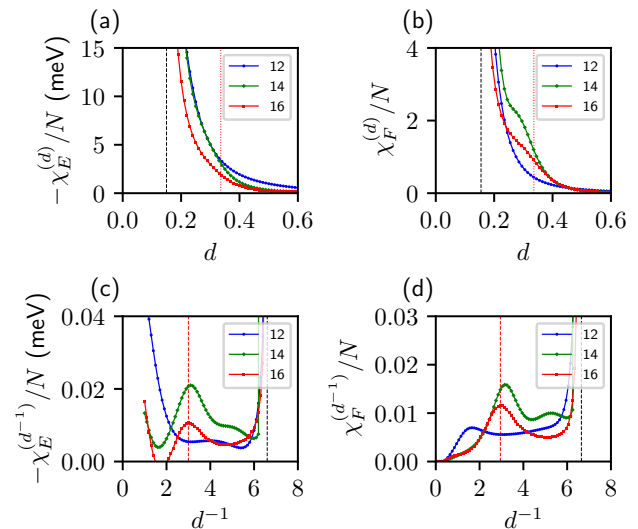


FIG. S6: **Ground State Energy and Wavefunction Fidelity Susceptibilities.** (a) Energy susceptibility and (b) Fidelity susceptibility of the lowest energy state in the $\mathbf{K} = 0$ sector as a function of d . (c,d) Same as (a,b) but as a function of d^{-1} . Across all (a-d), we identify $d_{c,1} \approx 0.15$ (black dashed line). For (c,d), we identify peaks at $d_{c,2} \approx 0.34$ (red dashed line). This transition point is marked on (a,b) as a red dotted line, and can be associated with a non-analytic feature of the fidelity susceptibility.

with $u = d$. Note that we use finite-difference approximations with $\delta d = 0.01$ to approximate the derivatives. For both the energy and fidelity susceptibilities, we can clearly identify a first-order transition at $d_{c,1}/a_M \approx 0.15$, which dominates the entire profile [Fig. S6(a,b)]. While no clear feature presents itself for the energy susceptibility, for the fidelity susceptibility, we can see a slight kink develop for $N = 14$ and 16 at $d_{c,2}/a_M \approx 0.34$ which warrants further investigation.

Note that d only enters the Hamiltonian through e^{-d} . As such, variations of physical observables with respect to d become progressively suppressed at larger d . Even more, since $d_{c,2} > d_{c,1}$, and the transition at $d_{c,1}$ is significantly stronger (first order) than $d_{c,2}$, the comparatively weaker signatures near $d_{c,2}$ are more easily obscured in a direct d -based representation. As such, let us attempt a reparameterization of the Hamiltonian and compute the susceptibilities using $u = d^{-1}$.

Let us now look at the susceptibilities using $u = d^{-1}$. We use finite-difference approximations with $\delta d^{-1} = 0.10$ to approximate the derivatives. For both the energy and fidelity susceptibilities, we can now observe a peak for $N = 14$ and 16 at $d_{c,2}/a_M \approx 0.34$ [Fig. S6(c,d)], consistent with the change in many-body spin Hall conductivity. The behavior is consistent with a continuous, likely second-order transition.

C. Extended Phase Space with Subtracted $V_0^{(1)}$

In this subsection, we consider the extended phase space with subtracted $V_0^{(1)}$ from the intervalley interaction. As a generalization to Eq. (2), we subtract the 0-th Haldane pseudopotential in the first Landau level contri-

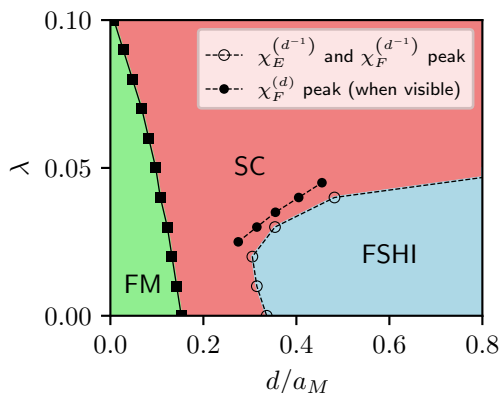


FIG. S7: **Extended Phase Diagram.** The FSHI-SC phase boundary is obtained using both the susceptibilities with respect to d^{-1} (empty black circles) and susceptibilities with respect to d (filled black circles). Only $\chi_F^{(d)}$ shows peaks for the latter, and only for the range $\lambda \in (0.025, 0.045)$.

bution to the intervalley interaction,

$$V^{\uparrow\downarrow}(\mathbf{p}) = \frac{e^2}{2\epsilon} \left[\frac{e^{-pd}}{p} - \lambda \ell_{BF} f\left(\frac{d}{\ell_B}\right) \left(1 - \frac{(\ell_B p)^2}{2}\right)^{-2} \right],$$

where $\lambda > 0$ is a dimensionless tuning parameter, and

$$f(a) = \int_0^\infty dx \left(1 - \frac{x^2}{2}\right)^2 e^{-x^2 - ax},$$

is a dimensionless function which monotonically decreases from $f(0) = \frac{11\sqrt{\pi}}{32}$ to $\lim_{a \rightarrow \infty} f(a) = 0$. We note that the equivalent of the parameter λ can be realized in the first moiré band by dielectric screening [14].

As this interaction does not affect the intravalley interaction while suppressing the intervalley interaction, it greatly suppresses the valley polarized IQHI relative to FSHI, while not having a significant impact on FSHI stability. It may have a small positive impact on FSHI stability at d close to $d_{c,2}$, especially at finite sizes, but this would be difficult to judge without more knowledge of the wavefunction. We do however expect the 0-th Haldane pseudopotential to have a significant impact on the stability of the superconductor. As the 0th-Haldane pseudopotential is predominantly the onsite interaction, its' subtraction generates an attractive BCS s -wave channel for the superconducting pairing to further minimize. As our pairing gap was evaluated to be the extended s -wave, it can naturally hybridize with this channel to enhance the stability of the superconductor, and as we increase λ , the pairing gap will naturally evolve into a fully gapped s -wave.

Calculating the extended phase diagram, we observe that even a small reduction of $\lambda < 0.1$ can completely suppress the ferromagnetic Chern insulator, and while it initially benefits the FSHI for $\lambda \lesssim 0.02$, it rapidly enhances the superconducting region for $\lambda \gtrsim 0.02$, quickly pushing the FSHI completely out of the experimentally relevant range of d [Fig. S7].

Moreover, as λ increases, the transition becomes more pronounced. Competing with the reduced effect of d on the interaction at larger d that we noted earlier, for $\lambda \in (0.025, 0.045)$, we were able to directly observe peaks in the fidelity susceptibility which we attribute to $d_{c,2}$. As an example, we plot the susceptibilities for $\lambda = 0.045$ [Fig. S8]. While these estimates for $d_{c,2}$ do not exactly coincide with those obtained from the susceptibilities with respect to d^{-1} due to finite size effects, their similarity is maximized at $\lambda \approx 0.03$ [Fig. S7], where the competing effects of the enhanced transition with λ and decreased scaling of d are likely maximized.

D. Additional Signatures of Superconductivity

In this subsection, we supplement the signatures of superconductivity in the intermediate regime. First, we

directly address the broken U(1) symmetry of superconductivity by checking if superconductivity is also stabilized at neighboring fillings $N_h = N \pm 2$, and by looking at the charge gap. Next, we supplement the binding energy $E_b^{(+)}$ [Fig. 3(b)] by presenting $E_b^{(-)}$, and the pair density matrix spectra for $N = 14$ [Fig. 3(c)] by presenting the same for $N = 16$. Then, we supplement the superfluid stiffness for $N = 14$ [Fig. 3(d)] by presenting the same for $N = 12$. Finally, we exclude exciton condensation as a possible explanation for the intermediate phase by looking at the spectra of excitonic pair density matrices.

a. Many-Body Gap at Neighboring Fillings and Charge Gap As SC is a compressible phase with broken U(1) symmetry, we naturally expect sufficiently small deviations in filling to preserve superconductivity. We also require the many-body ground state at such neighboring fillings to be of the same phase to compute the superconducting order parameter. Indeed, looking at the many-body gap for $N_h = N + 2$ holes, we identify a single ground state at $\mathbf{K} = 0$ around $d \in (d_{c,1}, d_{c,2})$ [Fig. S9(a)]. However, we observe that the many-body gap fully collapses for $N = 16$ [Fig. S9(b)]. This can be attributed to the broken particle-hole symmetry, and is indeed consistent with the particle-hole transformed band exhibiting greater dispersion [Fig. S2(c,d)]. As such, we have only compared $N_h = N$ with $N_h = N + 2$ for the superconducting order parameter [Fig. 4(a,b)].

We also consider the charge gap, which can be estimated from

$$\Delta_c = \frac{E_{N+2,0} + E_{N-2,0} - 2E_{N,0}}{2},$$

where $E_{N_h,0}$ is the ground-state energy for N_h holes. We find that the charge gap is minimized in the intermediate region, consistent with the intermediate phase having broken U(1) charge conservation, as opposed to the incompressible fractional spin Hall insulator [Fig. S9(c)].

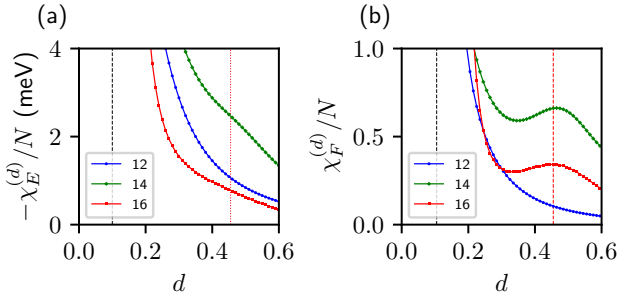


FIG. S8: Ground State Energy and Wavefunction Fidelity Susceptibilities at $\lambda = 0.045$. (a) Energy susceptibility and (b) Fidelity susceptibility of the lowest energy state in the $\mathbf{K} = 0$ sector as a function of d . We can identify a peak in the fidelity susceptibility at $d_{c,2} \approx 0.455$ (red dashed line in (b)). An associated dotted line is shown in (a) where a slight corresponding kink is visible.

Furthermore, for $N = 16$, we observe a crossover in the charge gap at $d_{c,2}$ from negative to positive, consistent with the transition from the compressible superconductor to the incompressible FSHI.

b. Binding Energy and Pair Density Matrix Spectra We note that while we include the Hartree correction when comparing energy for different magnetization sectors in [Fig. 1(b)], these are not included when computing the binding energy. This is because this correction is always positive and vanishes in the thermodynamic limit, so while it may add a better estimate to the binding energy at finite sizes, it is not meaningful in distinguishing transition behavior. The binding energy $E_b^{(-)}$ [Fig. S9(d)] exhibits largely similar trends to $E_b^{(+)}$ [Fig. 3(d)].

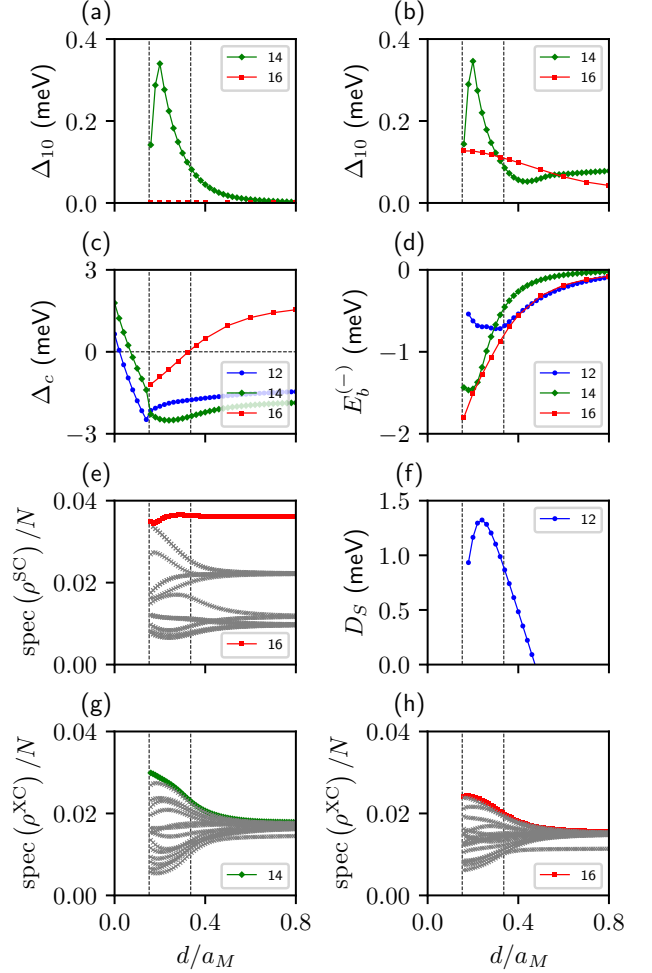


FIG. S9: Additional Signatures of Superconductivity. (a) Many-body gap $\Delta_{01} = E_1 - E_0$ at $N_h = N - 2$ filling. (b) Same as (a) at $N_h = N + 2$ filling. (c) Charge gap. (d) Binding energy, $E_b^{(-)}$. (e) Spectrum of the pair density matrix for $N = 16$. (f) Superfluid stiffness for $N = 12$. (g) Spectrum of the excitonic pair density matrix for $N = 14$. (h) Same as (g) for $N = 16$.

The spectra of the superconducting pair density matrix for $N = 16$ [Fig. S9(e)], similar to that of $N = 14$, also has a gapped first eigenvalue peaked in the intermediate region $d \in (d_{c,1}, d_{c,2})$, indicative of superconducting order. However, we note that it drops off much slower than $N = 14$ beyond $d_{c,2}$. While not presented, we also note that $N = 12$ follows a similar pattern to $N = 12$, rather than $N = 14$.

c. Superfluid Stiffness Superfluid stiffness was computed using the finite-difference method with $\delta\Phi = 0.01\Phi_0$. Let us now compare $N = 14$ [Fig. 3(d)] with $N = 12$ [Fig. S9(f)]. Unlike $N = 14$ which saw a monotonic decrease with d , for $N = 12$, the superfluid stiffness is maximized at an intermediate value within $(d_{c,1}, d_{c,2})$, rapidly drops off at a much faster rate around $d_{c,2}$, then attains a negative value for $d \gtrsim d_{c,2}$. The latter does not reflect upon a true instability, but is a finite-size effect from considering only one of the 36 degenerate ground states.

d. Excitonic Pair Density Matrix Spectra We consider the equivalent of the pair density matrix, Eq. (3), for excitonic pairs rather than Cooper pairs,

$$\rho_{\mathbf{k}'\mathbf{k}} = \left\langle \hat{X}_{\mathbf{k}'}^\dagger \hat{X}_{\mathbf{k}} \right\rangle_0, \quad \hat{X}_{\mathbf{k}}^\dagger = \hat{\psi}_{\uparrow,\mathbf{k}}^\dagger \hat{\psi}_{\downarrow,\mathbf{k}},$$

and similarly look to the spectrum as a function of d . We observe that for all $d > d_{c,1}$, the first eigenvalue remains close to the second eigenvalue [Fig. S9(g,h)], implying that exciton condensation fails to develop, and cannot explain the intermediate phase.

E. Additional Evidence of Superconducting Pairing Symmetry

In this subsection, we provide additional evidence for the observed superconducting pairing symmetry [Fig. 4(a,b)].

a. Maximal Pair Wavefunction The eigenvector of the pair density matrix, Eq. (3), corresponding to the

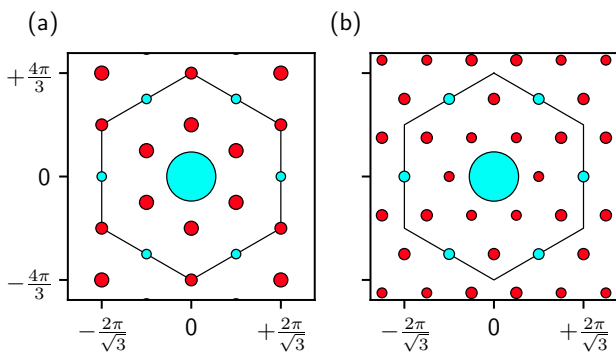


FIG. S10: **Maximal Pair Wavefunction.** Maximal pair wavefunction of Eq. (3) for (a) $N = 12$ and (b) 16 at $d/a_M = 0.28$.

first eigenvalue, also corresponds to the dominant pairing channel. As such, it provides an alternative means of probing the pairing symmetry of the superconducting state. We find that the maximal pair wavefunction [Fig. S10] indeed has the same pairing symmetries as the direct evaluation of the superconducting order parameter [Fig. 4(a,b)].

b. Adiabatic Connection to Ideal Extended s -Wave Superconductor We consider an ideal superconductor with the interaction,

$$V^{(\text{ideal})} = -U \left(\sum_{\mathbf{k}'} f(\mathbf{k}')^* \hat{\Delta}_{\mathbf{k}'} \right)^\dagger \left(\sum_{\mathbf{k}} f(\mathbf{k})^* \hat{\Delta}_{\mathbf{k}} \right),$$

where $f(\mathbf{k})$ is proportional to the desired SC order parameter. As a model extended s -wave, we use the maximal Cooper pair wavefunction for $f(\mathbf{k})$.

For a linear interpolation between the two interactions, $V^{(\lambda)} = (1 - \lambda)V^{(\text{Coulomb})} + \lambda V^{(\text{ideal})}$, where $V^{(\text{Coulomb})}$ is given by Eq. (2), we observe that the ground state remains gapped from the excited states [Fig. S11].

F. BCS vs. BEC

In this subsection, we discuss whether the intermediate superconductor is better described as being the BCS limit or the BEC limit.

At $d/a_M = 0.28$, the Fermi energy of the second moiré band is $E_F = 1.50$ meV. When using the particle-hole transformation of the second moiré band, the Fermi energy is enhanced to $E'_F = 2.70$ meV. This is comparable to the binding energy, which for $N = 16$ is $|E_b| = 1.37$ meV. This suggests the intermediate superconductor lies in the BCS-BEC crossover regime. Additionally, let us compare the superconducting coherence length (Section I.f) to the lattice constant a_M . As noted in the main text, the short coherence length also sug-

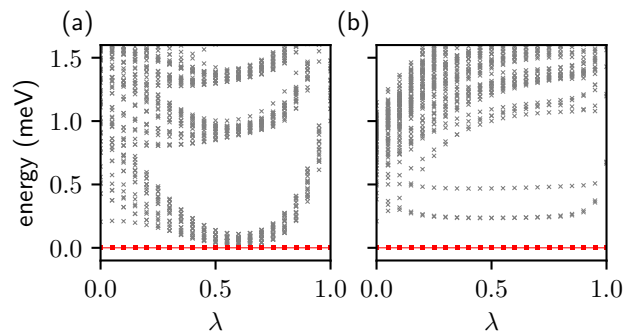


FIG. S11: **Adiabatic connection to ideal extended s -wave superconductor.** Evolution of the many-body spectrum for a linear interpolation between the Coulomb and ideal interactions for (a) $N = 12$ and (b) $N = 14$.

gests the intermediate superconductor lies in the BCS-BEC crossover regime, although direct numerical measurement of the coherence length must be carried out to make more definitive comparisons on this regard.

We note that many superconductors in moiré flat bands with non-trivial quantum geometry—magic-angle twisted bilayer graphene [15, 16], magic-angle twisted trilayer graphene [17, 18], and first moiré band chiral superconductivity in MoTe₂ [19]—have been suggested to exhibit BEC–BCS crossover characteristics. These indications are based on analyses of the superconducting coherence length [16, 17, 19], the ratio $|E_b|/E_F$ [15, 18], the relation between T_{BKT} , E_F , and $|E_b|$ [15, 17, 20], as well as observations of pseudogap behavior [15, 18].

III. INTERMEDIATE SUPERCONDUCTIVITY IN GENERALIZED FIRST LANDAU LEVELS

a. First Landau Levels Let us define a model consisting of a first Landau level and its time-reversal conjugate [6]. The non-interacting energies have no dispersion, so without loss of generality, we set them as zero. For the interaction, we again use Eq. (S1), but replace the form factors for those of the first Landau level,

$$f_{\mathbf{k},\mathbf{P}}^s = \eta_{|\mathbf{k}+\mathbf{P}|} L_1 \left(\frac{1}{2} \ell_B^2 \|\mathbf{P}\|^2 \right) \times e^{-\frac{1}{4} \ell_B^2 \|\mathbf{P}\|^2 - \frac{i}{2} s \ell_B^2 \hat{\mathbf{z}} \cdot (\mathbf{P} \times \mathbf{k} - \{\mathbf{k}+\mathbf{P}\} \times \{\mathbf{k}+\mathbf{P}\})},$$

where $L_1(x)$ is the first Laguerre polynomial and $\eta_{\bullet} : \hat{\Lambda} \rightarrow \{\pm 1\}$ is a sign factor defined by taking some representation of the reciprocal lattice $\hat{\Lambda} = \text{span}_{\mathbb{Z}}(\mathbf{q}_1, \mathbf{q}_2)$ and setting $\eta_{l_1 \mathbf{q}_1 + l_2 \mathbf{q}_2} = (-1)^{l_1 + l_2 + l_1 l_2}$, i.e. only +1 when l_1 and l_2 are both even, and -1 otherwise.

b. Generalized First Landau Levels We use a generalization of first Landau level wavefunctions given by

$$\psi_{\mathbf{k}}(\mathbf{r}) = \mathcal{N}_{\mathbf{k}} e^{i\phi(\mathbf{r})} \psi_{\mathbf{k}}^{(\text{1LL})}(\mathbf{r}),$$

where $\mathcal{N}_{\mathbf{k}}$ is a normalization factor, and $\phi(\mathbf{r})$ is a lowest harmonic modulation which preserves the lattice symmetries,

$$\phi(\mathbf{r}) = \frac{\sqrt{3}}{4\pi} K \sum_i \cos(\mathbf{Q}_i \cdot \mathbf{r}),$$

with a parameter K which controls the strength of the modulation.

We note that a similar generalization for LLLs has been often used in context of quantum geometry to introduce non-uniformity while maintaining ideality [21–23], and was recently used to stabilize chiral superconductivity proximate to the $\nu_h = \frac{2}{3}$ fractional quantum anomalous Hall state [24].

c. Many-Body Spectra When considering exact first Landau levels ($K = 0$), for $N = 14$, we observe that

the many-body spectrum evolves directly from the ferromagnetic Chern insulator to the fractional spin Hall insulator [Fig. S12]. Introducing non-uniform quantum geometry with $K = 0.1$, the many-body spectrum exhibits the singular ground state at $d = 0.28$ [Fig. S13(a,b)],

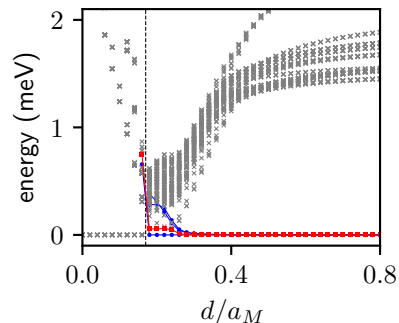


FIG. S12: Evolution of many-body spectra for the ideal first Landau level and its time reversal conjugate for $N = 14$. The states connecting to the ground states of the fractional spin Hall insulator in the $d \rightarrow \infty$ limit are colored (red square or blue circle). We do not observe the intermediate state with a singular gapped state with total momentum $K = 0$ (red squares), which is instead, immediately degenerate with the state with total momentum $K = 7$.

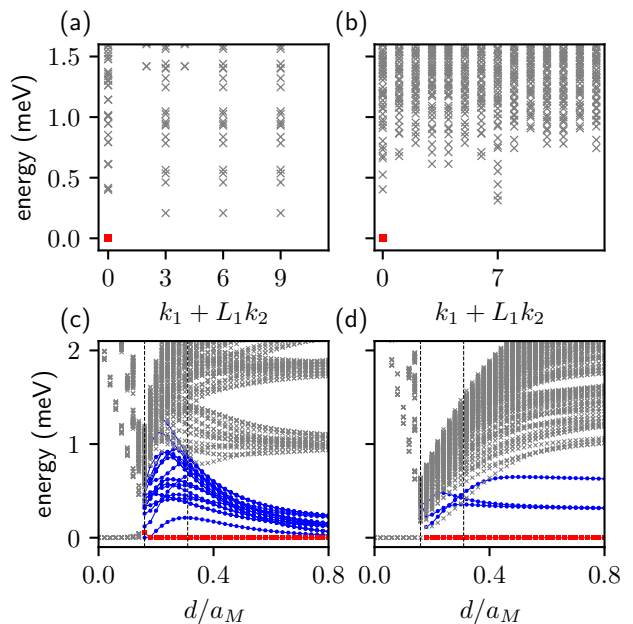


FIG. S13: Many-body spectra for a generalized first Landau level and its time reversal conjugate. (a,b) Many-body spectrum at $d = 0.28$ for $N = 12$ and 14 , respectively. (c,d) Evolution of the many-body spectra over d for $N = 12$ and 14 , respectively.

and the overall evolution of the spectra become highly similar to that of the continuum model of twisted bilayer MoTe₂ [Fig. S13(c,d)]. This suggests non-uniform quantum geometry is a key ingredient in stabilizing the intermediate superconductor.

IV. KOHN-LUTTINGER MECHANISM FOR THE INTERMEDIATE SUPERCONDUCTOR

a. Random Phase Approximation Here we present the random phase approximation, incorporating quantum geometry and spin anisotropy. The screened interaction is given by

$$\begin{aligned} \bar{V}^{ss'}(\mathbf{p}; \mathbf{Q}, \mathbf{Q}') \\ = \sum_{\bar{s}} \left[(\mathbf{I} + \mathbf{Z}_{\mathbf{p}})^{-1} \right]_{(s, \mathbf{Q}), (\bar{s}, \mathbf{Q}')} V^{\bar{s}s'}(\mathbf{p} + \mathbf{Q}'), \end{aligned}$$

where \mathbf{I} and $\mathbf{Z}_{\mathbf{p}}$ are dimensionless matrices with indices in $\mathbb{Z}_2^{\text{spin}} \times \hat{\Lambda}$. \mathbf{I} is the identity matrix, and $\mathbf{Z}_{\mathbf{p}}$ is given by

$$[\mathbf{Z}_{\mathbf{p}}]_{(s, \mathbf{Q}), (s', \mathbf{Q}')} = V^{ss'}(\mathbf{p} + \mathbf{Q}) \chi_{\mathbf{p}, \mathbf{Q} \mathbf{Q}'}^s,$$

and $\chi_{\mathbf{p}, \mathbf{Q} \mathbf{Q}'}^s$ is the quantum geometry weighted static polarization,

$$\chi_{\mathbf{p}, \mathbf{Q} \mathbf{Q}'}^s = \frac{1}{A} \sum_{\mathbf{k}} \bar{f}_{\mathbf{k}, \mathbf{p} + \mathbf{Q}}^s \bar{f}_{\mathbf{k}, \mathbf{p} + \mathbf{Q}'}^s \tau_{\mathbf{k}, \mathbf{p}}^s,$$

where

$$\tau_{\mathbf{k}, \mathbf{p}}^s = - \frac{\left(1 + e^{(\epsilon_{\{\mathbf{k} + \mathbf{p}\}}^s - \mu)/T} \right)^{-1} - \left(1 + e^{(\epsilon_{\mathbf{k}}^s - \mu)/T} \right)^{-1}}{\epsilon_{\{\mathbf{k} + \mathbf{p}\}}^s - \epsilon_{\mathbf{k}}^s}.$$

Note that due to the ambiguity of momentum up to reciprocal lattice momentum under the creation and annihilation of electron-hole pairs, it is possible $\mathbf{Q} \neq \mathbf{Q}'$.

In twisted bilayer MoTe₂ second moiré bands, the first Landau level-like quantum geometry implies the form factors decay exponentially at the rate of the magnetic length. As such, the static polarization can be reasonably approximated as diagonal along the reciprocal lattice index,

$$\chi_{\mathbf{p}, \mathbf{Q} \mathbf{Q}'}^s \approx \delta_{\mathbf{Q} \mathbf{Q}'} \chi_{\mathbf{p} + \mathbf{Q}}^s,$$

where

$$\chi_{\mathbf{P}}^s = \frac{1}{A} \sum_{\mathbf{k}} |\bar{f}_{\mathbf{k}, \mathbf{P}}^s|^2 \tau_{\mathbf{k}, \{\mathbf{P}\}}^s.$$

The screened interaction is then expressed as a potential,

$$\bar{V}^{ss'}(\mathbf{P}) = \sum_{\bar{s}} \left[(\mathbf{I} + \mathbf{Z}_{\mathbf{P}})^{-1} \right]_{s\bar{s}} V^{\bar{s}s'}(\mathbf{P}), \quad (\text{S2})$$

where \mathbf{I} is the 2×2 identity matrix over spin and

$$[\mathbf{Z}_{\mathbf{P}}]^{ss'} = V^{ss'}(\mathbf{P}) \chi_{\mathbf{P}}^{s'}.$$

We use this expression for our calculations.

b. RPA Screening in tbMoTe₂ Second Moiré Bands We have calculated the RPA-screened intervalley interaction for the second moiré bands at $d/a_M = 0.28$ [Fig. 4(c)]. Here we elaborate on various contributing factors listed in the main text.

As discussed in Section I.d, because the second moiré band has non-uniform quantum geometry and is very flat relative to the interaction strength, it is non-trivially renormalized under particle-hole transformation [Fig. S2(c,d)]. In addition to increasing the bandwidth, while the original band has only a single Fermi surface pocket, the particle-hole transformed band has three Fermi surface pockets. The presence of multiple Fermi surface pockets have been argued to be beneficial in stabilizing Kohn-Luttinger superconductivity [25], and is likely relevant for $\nu_h \gtrsim 3$. Additionally, the second moiré band hosts van Hove singularities at the μ points, which are close to the $\nu_h = 3$ Fermi surface, which even change occupation of the μ points under particle-hole transformation [Fig. S2(c,d)]. As the van Hove singularities have divergent density of states, they provide large leading contribution to the static polarization, and thus, significant RPA screening [26, 27].

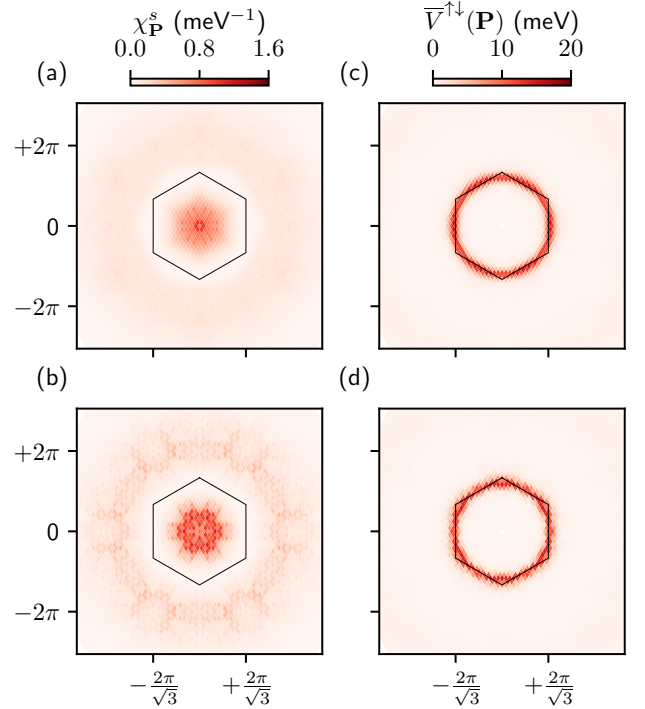


FIG. S14: **RPA Screened Intervalley Interaction.**

(a,b) Static polarization using (a) the second moiré band at $\nu_h = 2$, (b) and the particle-hole transformed band, for $d/a_M = 0.28$. Due to time-reversal and valley-reduced inversion symmetry, the static polarizations are the same for both valleys. (c,d) The respective RPA screened intervalley interaction potential.

Let us now discuss the static polarization, $\chi_{\mathbf{P}}^s$ [Fig. S14(a,b)]. We note that both spins give the same expression for the static polarization. For both the electron and hole basis, we observe similar overall radial features in $\chi_{\mathbf{P}}^s$. It is largest at small $\|\mathbf{P}\|$, quickly decreases in magnitude and attains a minima at the edges of the first Brillouin zone, $\|\mathbf{P}\| \sim Q/2$ where $Q = \|\mathbf{Q}_1\|$, then increases again to attain a much smaller maxima at $\|\mathbf{P}\| \sim Q$, and so forth. There are also non-trivial C_3^z -symmetric angular features, which are much more pronounced for the particle-hole transformed band. The rapid decay of the static polarization with \mathbf{P} can primarily be attributed to the first Landau level like character of the second moiré band, while the non-trivial radial and angular features result from non-uniform quantum geometry and Fermi surface pockets. In particular, it has been noted that if the quantum geometry is uniform, or more generally, if the quantum distance along the Fermi surface is in some sense equal to the quantum geometry-driven under-screening driven by the form factors between the Fermi sea and complementary unoccupied states, the two effects can cancel out, resulting in a monotonically decreasing static polarization. This occurs in exactly uniform setups such as spin-polarized Landau levels [28].

Substituting the static polarization into Eq. (S2), we obtain the RPA screened intervalley interaction [Fig. S14(c,d)]. We note that due to spin anisotropy of the bare interaction, Eq. (2), the intervalley interaction is more strongly screened than the intravalley interaction. Unlike the bare intervalley interaction, which monotonically decreases with $\|\mathbf{P}\|$, the RPA screened intervalley interaction *increases* in momentum within the first Brillouin zone, attaining a maxima along its' edges $\|\mathbf{P}\| \approx Q/2$, before dropping off. This is true for both the electron and hole basis. Such behavior is highly desirable for stabilizing Kohn-Luttinger superconductivity, and typically leads to nodal superconductivity [28]. As such, the non-uniform quantum geometry is a critical ingredient for the Kohn-Luttinger mechanism in quantum geometry driven superconductivity. The two bases differ in the C_3^z angular features, with the particle-hole transformed band exhibiting a greater amplitude to the C_3^z angular features, likely further stabilizing Kohn-Luttinger superconductivity.

c. Linearized BCS Gap Equation and Kohn-Luttinger Pairing Instability At the mean-field level, the superconducting gap satisfies the BCS self-consistent gap equation,

$$\Delta_{\mathbf{k}} = -\frac{1}{2A} \sum_{\mathbf{k}'} \mathfrak{V}_{\mathbf{k}\mathbf{k}'} \frac{\tanh(\xi_{\mathbf{k}'}/2T)}{\xi_{\mathbf{k}'}} \Delta_{\mathbf{k}'},$$

where $\mathfrak{V}_{\mathbf{k}\mathbf{k}'}$ is the reduced interaction matrix,

$$\mathfrak{V}_{\mathbf{k}\mathbf{k}'} = \sum_{\mathbf{Q}} \left| \hat{f}_{\mathbf{k}', \mathbf{k}-\mathbf{k}'+\mathbf{Q}}^\dagger \right|^2 \tilde{V}^{\uparrow\downarrow}(\mathbf{k}-\mathbf{k}'+\mathbf{Q}).$$

and $\xi_{\mathbf{k}} = \sqrt{(\epsilon_{\mathbf{k}} - \mu)^2 + \Delta_{\mathbf{k}}^2}$ gives the energy of the Bogoliubov quasiparticles. We solved the linearized BCS gap equation for the RPA screened intervalley interaction to determine the pairing instability [Fig. 4(d)].

d. Limitations of Kohn-Luttinger Analysis We note that, although we obtain a nodal extended *s*-wave pairing instability in the A_1 irreducible representation—consistent with the pairing symmetry found in the exact diagonalization calculations—some discrepancies remain, such as the sign reversal of the pairing function between the γ and μ points. We attribute such deviations to the limitations of the Kohn-Luttinger pairing instability, which is derived within a mean-field and perturbative framework, whereas in our system the Coulomb interaction exceeds the bandwidth and the superconducting state resides in the BCS-BEC crossover regime (Section II.F), where strong interactions beyond perturbative treatments become important.

V. FIELD-THEORETICAL DESCRIPTION OF THE FSHI-SC TRANSITION

In this section, we provide additional details on our field-theoretical description of the transition from the fractional spin Hall insulator to the superconductor.

a. Effective Field Theory of the Fractional Spin Hall Insulator The fractional spin Hall insulator can be viewed as a time-reversal symmetric pair of the Pfaffian states, i.e., $\text{Pf} \times \overline{\text{Pf}}$. The effective field theory of the Pfaffian state is [29]

$$\begin{aligned} \mathcal{L}_{\text{Pf}} = & -\frac{2}{4\pi} \text{Tr} \left(a da + \frac{2}{3} a^3 \right) + \frac{3}{4\pi} (\text{Tr} a) d(\text{Tr} a) \\ & + \frac{1}{2\pi} A d \text{Tr} a + \frac{1}{4\pi} A dA + 2\text{CS}_g, \end{aligned}$$

where a is a dynamical U(2) gauge field, A is the background electromagnetic field, and CS_g is the gravitational Chern-Simons term. Its time-reversal conjugate is given by

$$\begin{aligned} \mathcal{L}_{\overline{\text{Pf}}} = & \frac{2}{4\pi} \text{Tr} \left(a da + \frac{2}{3} a^3 \right) - \frac{3}{4\pi} (\text{Tr} a) d(\text{Tr} a) \\ & - \frac{1}{2\pi} A d \text{Tr} a - \frac{1}{4\pi} A dA - 2\text{CS}_g. \end{aligned}$$

Thus, the total Lagrangian describing the fractional spin Hall insulator is

$$\begin{aligned} \mathcal{L}_{\text{FSHI}} = & -\frac{2}{4\pi} \text{Tr} \left(a da + \frac{2}{3} a^3 \right) + \frac{3}{4\pi} (\text{Tr} a) d(\text{Tr} a) \\ & + \frac{2}{4\pi} \text{Tr} \left(b db + \frac{2}{3} b^3 \right) - \frac{3}{4\pi} (\text{Tr} b) d(\text{Tr} b) \\ & + \frac{1}{2\pi} A d(\text{Tr} a - \text{Tr} b), \end{aligned} \quad (\text{S3})$$

where b is another dynamical U(2) gauge field. The Lagrangian Eq. (S3) describes the topological order of the fractional spin Hall insulator, which is given by $\text{Pf} \times \overline{\text{Pf}}$.

b. Anyon Condensation Transition The transition to the superconductor is induced by the condensation of a complex scalar field Φ that transforms as the bifundamental representation of $U(2) \times U(2)$, whose covariant derivative is given by

$$D_\mu \Phi = \partial_\mu \Phi - i \sum_{l=0}^3 (a_\mu^l T^l \Phi + b_\mu^l \Phi T^l),$$

where $T^0 = I/2$ and $T^l = \sigma^l/2$ are the generators of the Lie algebra $\mathfrak{u}(2)$. The scalar field Φ is identified as the composite of the charge- $\frac{1}{4}$ non-Abelian anyon $\sigma_{\frac{1}{4}}$ in the Pfaffian state Pf and its time-reversed partner $\sigma_{\frac{1}{4}}^T$ in the time-reversed Pfaffian state $\overline{\text{Pf}}$. Anyons in $U(2)$ Chern-Simons theory are labeled by (j, n) with $j + \frac{n}{2} \in \mathbb{Z}$, where $2j$ and n are integers [30]. Here, j and n correspond to an irreducible representation of $SU(2)$ and a charge of $U(1)$, respectively. In this framework, Φ corresponds to the composite of the anyons labeled $(\frac{1}{2}, 1)$ in Pf and $(\frac{1}{2}, 1)$ in $\overline{\text{Pf}}$. The anyon $(\frac{1}{2}, 1)$ in Pf can be identified with the charge- $\frac{1}{4}$ non-Abelian anyon $\sigma_{\frac{1}{4}}$. To further demonstrate consistency, we check the electric charge of the anyon. The Abelian sector of Pf, associated with the gauge field a , is described by a $U(1)_8$ theory. Including the coupling to the external electromagnetic gauge field A , this Abelian sector can be represented by the K -matrix $K = (8)$ and the charge vector $\mathbf{t} = (2)$. The electric charge of an anyon labeled by integer vector $\mathbf{l} = (1)$ is then given by $q_{\mathbf{l}} = \mathbf{t}^T K^{-1} \mathbf{l} = \frac{1}{4}$.

When the gauge-invariant operator $\text{Tr } \Phi^\dagger \Phi$ acquires a finite vacuum expectation value, i.e., $\langle \text{Tr } \Phi^\dagger \Phi \rangle \neq 0$, the $U(2) \times U(2)$ gauge group is spontaneously broken. To understand how the condensation reduces the gauge group, we denote the singular values of Φ by s_1 and s_2 . Expressed in terms of these singular values, the potential energy $V(\Phi^\dagger \Phi)$ in our Chern-Simons-Landau-Ginzburg theory takes the form

$$\begin{aligned} V &= m^2 \text{Tr } \Phi^\dagger \Phi + \lambda_1 \text{Tr } \Phi^\dagger \Phi \Phi^\dagger \Phi + \lambda_2 (\text{Tr } \Phi^\dagger \Phi)^2 \\ &= m^2 (s_1^2 + s_2^2) + \frac{\lambda_1 + \lambda_2}{2} (s_1^2 + s_2^2)^2 + \frac{\lambda_1}{2} (s_1^2 - s_2^2)^2. \end{aligned}$$

For our purposes, we take $m^2 < 0$ to ensure condensation, and impose $\lambda_1 > 0$ and $\lambda_1 + \lambda_2 > 0$ to guarantee that the potential energy is bounded from below. The potential energy $V(\Phi^\dagger \Phi)$ is minimized when the singular values are equal as $s \equiv s_1 = s_2$, with

$$s = \sqrt{\frac{-m^2}{2(\lambda_1 + \lambda_2)}}.$$

Choosing a gauge in which the condensate takes the form $\langle \Phi \rangle = sI$ with $s > 0$, the kinetic term becomes

$$\text{Tr} (D^\mu \langle \Phi \rangle^\dagger D_\mu \langle \Phi \rangle) = \frac{s^2}{2} \sum_{l=0}^3 (a_\mu^l + b_\mu^l)^2.$$

This shows that, in the condensed phase, the combination $a_\mu + b_\mu$ acquires a mass, effectively imposing the constraint $\alpha \equiv a = -b$ at low energies. Substituting this into the Lagrangian Eq. (S3), we obtain the effective field theory describing the superconductor [31],

$$\mathcal{L}_{\text{SC}} = \frac{2}{2\pi} A \text{d Tr } \alpha. \quad (\text{S4})$$

Transitions of this type have been extensively studied in literature and are widely believed to be continuous [32–45], supported by both field-theoretical arguments [32–40] and numerical studies [40–45].

c. Effective Field Theory of the Superconductor We now discuss Eq. (S4) in more detail, showing that it indeed describes a charge- $2e$ superconductor. Consider an arbitrary closed 2-manifold Σ_2 and cover it with two open patches N and S , which overlap at the “equator” $E \simeq S^1$. In the overlap region E , the locally defined $U(2)$ gauge fields α_N and α_S are related by a gauge transformation

$$\alpha_N = g^{-1} \alpha_S g - i g^{-1} dg,$$

where $g : E \rightarrow U(2)$. Taking the trace, we get

$$\text{Tr } \alpha_N = \text{Tr } \alpha_S - i \text{d}(\log \det g),$$

where we have used the identity $\text{Tr } g^{-1} dg = \text{d}(\log \det g)$. Then, by integrating $\text{d Tr } \alpha$ over Σ_2 , we get

$$\int_{\Sigma_2} \text{d Tr } \alpha = - \int_E \text{d}(\log \det g).$$

Note that $\det g$ maps $E \simeq S^1$ into $U(1)$. Since the integral of the derivative of the logarithm of a map $S^1 \rightarrow U(1)$ is given by $2\pi i$ times the winding number of the map, we have

$$\int_{\Sigma_2} \text{d Tr } \alpha \in 2\pi\mathbb{Z}.$$

Thus, the flux of $\text{Tr } \alpha$ is quantized in 2π . Since there is no Chern-Simons term, the 2π monopole of $\text{Tr } \alpha$, which is bound to the $SU(2)$ π -flux, is gauge-invariant, and can condense and lead to the confinement. In the absence of gapless matter fields coupled to the gauge fields, and in the absence of topological terms (recall that A is a non-dynamical background gauge field and thus the mutual Chern-Simons coupling to A does not generate a mass term for the dynamical gauge fields), the gauge field α is expected to be confining [46, 47], corresponding to the superconducting state of interest. Since the mutual Chern-Simons level between A and $\text{Tr } \alpha$ is 2, the condensation of the monopole induces charge- $2e$ superconductivity.

d. Additional Details of the Condensation Transition To complete the analysis, we will show that all 8 components of Φ are either eaten by the massive vector fields or gapped. To see which components are eaten, we express Φ as

$$\Phi = e^{i\theta^a T^a / s} (sI + H)$$

using the polar decomposition. Here, θ^a are 4 real phase fields and H is a 2×2 Hermitian matrix. Note that H also contains 4 real scalar fields, so that the total degrees of freedom of Φ is 8 as expected. Since every unitary matrix can be written as the square of another unitary matrix, the scalar field can be written as a Hermitian matrix via a gauge transformation. Note that 4 degrees of freedom θ^a have been absorbed into the redefinition of the gauge fields, or “eaten” by the gauge fields. With this gauge choice, the scalar field can be written as

$$\Phi = \begin{pmatrix} s + \sigma_1 & x - iy \\ x + iy & s + \sigma_2 \end{pmatrix},$$

where σ_j , x , and y are real scalar fields. Note that these four fields correspond to the remaining uneaten components of Φ . By plugging this into the potential energy, we get

$$\begin{aligned} V = & 4s^2(\lambda_1 - s(\lambda_1 + \lambda_2))(\sigma_1 + \sigma_2) \\ & + 2s^2(2\lambda_1 + \lambda_2)(\sigma_1^2 + \sigma_2^2) \\ & + 8s^2\lambda_1(x^2 + y^2) + \dots, \end{aligned}$$

where \dots includes higher-order terms. We find that all four real scalar fields acquire a finite mass. Specifically, the mass of σ_j are $2s\sqrt{2\lambda_1 + \lambda_2}$, while the mass of x and y are $4s\sqrt{\lambda_1}$. Thus, in the effective Lagrangian, these components are gapped out and do not appear.

VI. CATEGORICAL DESCRIPTION OF THE FSHI-SC TRANSITION

In this section, we supplement our field-theoretical argument, which is on its own sufficient and self-contained, with a category-theoretic formulation of anyon superconductivity developed by some of our authors [48], and show that the results are consistent. Within this framework, anyon superconductivity is understood as a generalized anyon condensation that explicitly keeps track of charge conservation, and the breaking of charge conservation.

a. General Categorical Description of Anyon-Driven Superconductivity Topological orders in $2 + 1$ dimensions host exotic quasiparticles known as anyons and the anyon theories are classified by modular tensor categories [49, 50]. When a given topological order has global $U(1)$ charge conservation symmetry, the anyons carry fractionalized electric charges [51]. Although the fractional charges of the anyons are captured modulo e in the standard modular tensor category formalism, to fully describe the transition into a superconducting phase via anyon condensation, it is necessary to track the exact values of the anyon charges.

To do so, modular tensor categories over $\text{Rep}(U(1))$ or $\text{sRep}(U(1)^f)$ are introduced in Ref. [48]. The subcategories $\text{Rep}(U(1))$ and $\text{sRep}(U(1)^f)$ describes the local excitations, i.e., those do not exhibit anyonic statistics, carrying integer-valued electric charges in units of e . The

fractional charges of the anyons are determined by their fusion rules involving these local excitations. Then, the transition into a superconductor is described by a condensable algebra \mathcal{A} , which represents condensing anyons during the transition. When the anyons in \mathcal{A} are charged, then \mathcal{A} must contain charged local excitations since \mathcal{A} includes at least one fusion channel of its constituent anyons. In consequence, the condensation of \mathcal{A} breaks $\text{Rep}(U(1))$ or $\text{sRep}(U(1)^f)$ down to a smaller subcategory. Physically, this means that the global $U(1)$ charge conservation symmetry is broken down to a subgroup, implying that a superconducting phase emerges. The charge quantization of the resulting superconductor is determined by the smallest local charge included in \mathcal{A} .

More precisely, the category $\text{Rep}(U(1))$ consists of a countably infinite number of simple objects, labeled by integers $\dots, \bar{2}, \bar{1}, \mathbf{0}, \mathbf{1}, \mathbf{2}, \dots$. Physically, the integers correspond to conserved $U(1)$ charges of local particle-like excitations. All the simple objects braid trivially with one another and have bosonic self-statistics. While the category $\text{sRep}(U(1)^f)$ also consists of integer-labeled simple objects, the odd-integer objects now have fermionic self-statistics. This can be viewed as a categorical implementation of the spin-charge relation [52], which is obeyed in ordinary condensed matter composed of electrons. When the condensable algebra \mathcal{A} contains a local boson \mathbf{m} , the condensation of \mathcal{A} imposes the equivalence relation $\mathbf{n} \sim \mathbf{n} + \mathbf{m}$ to the integer-labeled objects. In consequence, $U(1)$ charges of the local excitations are defined only modulo \mathbf{m} in the condensed phase. Categorically, $\text{Rep}(U(1))$ (or $\text{sRep}(U(1)^f)$) is mapped into $\text{Rep}(\mathbb{Z}_m)$ (or $\text{sRep}(\mathbb{Z}_m^f)$) due to the condensation of \mathcal{A} , which describe onsite \mathbb{Z}_m symmetries [53]. Thus, the above process can be viewed as a categorical description of symmetry breaking $U(1)$ down to \mathbb{Z}_m , which induces charge- me superconductivity [48].

b. Categorical Description of the FSHI-SC Transition Now, let us apply the above categorical formalism to the transition from the fractional spin Hall state $\text{Pf} \times \overline{\text{Pf}}$ to the charge- $2e$ superconductor. We first recall that the Pfaffian state contains six distinct anyon types, labeled by $\mathbf{0}$, $\sigma_{\frac{1}{4}}$, ψ_0 , $\alpha_{\frac{1}{2}}$, $\bar{\sigma}_{\frac{3}{4}}$, and $\bar{\alpha}_{\frac{1}{2}}$, where the subscripts denote their electric charges in units of the electron charge e (with $\mathbf{0}$ representing the vacuum sector) [50]. The mutual statistics of the anyons are encoded in the (fermion-quotient) S matrix [50]:

$$S = \frac{1}{2\sqrt{2}} \begin{pmatrix} 1 & \sqrt{2} & 1 & 1 & \sqrt{2} & 1 \\ \sqrt{2} & 0 & -\sqrt{2} & i\sqrt{2} & 0 & -i\sqrt{2} \\ 1 & -\sqrt{2} & 1 & 1 & -\sqrt{2} & 1 \\ 1 & i\sqrt{2} & 1 & -1 & -i\sqrt{2} & -1 \\ \sqrt{2} & 0 & -\sqrt{2} & -i\sqrt{2} & 0 & i\sqrt{2} \\ 1 & -i\sqrt{2} & 1 & -1 & i\sqrt{2} & -1 \end{pmatrix}.$$

More precisely, the mutual braiding phase of a pair of anyons i and j are given by $S_{ij}^* S_{11} / S_{1i} S_{1j}$ [51]. In a $U(2)$ gauge theory [30], these anyons correspond respectively to $(k = 0, n = 0)$, $(\frac{1}{2}, 1)$, $(1, 0)$, $(0, 2)$, $(\frac{1}{2}, 3)$, and $(1, 2)$.

The anyon content of the time-reversal-conjugate consists of the corresponding time-reversed partners: $\mathbf{0}$, $\sigma_{\frac{1}{4}}^{\mathcal{T}}$, $\psi_0^{\mathcal{T}}$, $\alpha_{\frac{1}{2}}^{\mathcal{T}}$, $\bar{\sigma}_{\frac{3}{4}}^{\mathcal{T}}$, and $\bar{\alpha}_{\frac{1}{2}}^{\mathcal{T}}$. The mutual braiding statistics of the time-reversed anyons can be simply obtained by taking complex conjugation on the mutual statistics of the anyons in the Pfaffian theory. Since we are considering a bilayer system where each layer host the Pfaffian theory and its time-reversal, any pair of anyons consisting of one from the Pfaffian and the other from the time-reversed Pfaffian always braid trivially. Therefore, the full anyon content of the fractional quantum spin Hall state, described by $\text{Pf} \times \overline{\text{Pf}}$, consists of all composite pairs formed by combining anyons from Pf and those from $\overline{\text{Pf}}$.

The transition described by the field-theoretical framework above corresponds to an anyon condensation characterized by the condensable algebra

$$\mathcal{A} = \bigoplus_{\mathbf{m} \in 2\mathbb{Z}} \mathbf{m} \cdot \left(\mathbf{0} \oplus \psi_0 \psi_0^{\mathcal{T}} \oplus \sigma_{\frac{1}{4}} \sigma_{\frac{1}{4}}^{\mathcal{T}} \oplus \alpha_{\frac{1}{2}} \alpha_{\frac{1}{2}}^{\mathcal{T}} \oplus \bar{\alpha}_{\frac{1}{2}} \bar{\alpha}_{\frac{1}{2}}^{\mathcal{T}} \oplus \bar{\sigma}_{\frac{3}{4}} \bar{\sigma}_{\frac{3}{4}}^{\mathcal{T}} \right).$$

Note that the fusion rules of the anyons are given by

$$\begin{aligned} \sigma_{\frac{1}{4}} \otimes \sigma_{\frac{1}{4}} &= \alpha_{\frac{1}{2}} \oplus \bar{\alpha}_{\frac{1}{2}}, \\ \sigma_{\frac{1}{4}} \otimes \alpha_{\frac{1}{2}} &= \sigma_{\frac{1}{4}} \otimes \bar{\alpha}_{\frac{1}{2}} = \bar{\sigma}_{\frac{3}{4}}, \\ \sigma_{\frac{1}{4}} \otimes \bar{\sigma}_{\frac{3}{4}} &= \mathbf{1} \oplus \mathbf{1}\psi_0, \\ \alpha_{\frac{1}{2}} \otimes \alpha_{\frac{1}{2}} &= \bar{\alpha}_{\frac{1}{2}} \otimes \bar{\alpha}_{\frac{1}{2}} = \mathbf{1}\psi_0, \\ \alpha_{\frac{1}{2}} \otimes \bar{\alpha}_{\frac{1}{2}} &= \mathbf{1}, \\ \alpha_{\frac{1}{2}} \otimes \bar{\sigma}_{\frac{3}{4}} &= \bar{\alpha}_{\frac{1}{2}} \otimes \bar{\sigma}_{\frac{3}{4}} = \mathbf{1}\sigma_{\frac{1}{4}}. \end{aligned}$$

The fusion rules of the time-reversed anyons with the superscript \mathcal{T} are given as the same. Therefore, all the anyons in \mathcal{A} appear in the repeated fusion of $\sigma_{\frac{1}{4}} \sigma_{\frac{1}{4}}^{\mathcal{T}}$. For example,

$$\begin{aligned} (\sigma_{\frac{1}{4}} \sigma_{\frac{1}{4}}^{\mathcal{T}})^2 &\supset \alpha_{\frac{1}{2}} \alpha_{\frac{1}{2}}^{\mathcal{T}} \oplus \bar{\alpha}_{\frac{1}{2}} \bar{\alpha}_{\frac{1}{2}}^{\mathcal{T}}, \\ (\sigma_{\frac{1}{4}} \sigma_{\frac{1}{4}}^{\mathcal{T}})^3 &\supset \bar{\sigma}_{\frac{3}{4}} \bar{\sigma}_{\frac{3}{4}}^{\mathcal{T}}, \\ (\sigma_{\frac{1}{4}} \sigma_{\frac{1}{4}}^{\mathcal{T}})^4 &\supset \mathbf{2} \oplus \mathbf{2}\psi_0, \\ (\sigma_{\frac{1}{4}} \sigma_{\frac{1}{4}}^{\mathcal{T}})^4 &\otimes \bar{\mathbf{2}} \supset \mathbf{0} \oplus \psi_0. \end{aligned}$$

Since \mathcal{A} contains the charge- $2e$ local boson $\mathbf{2}$, the condensation of \mathcal{A} breaks $\text{sRep}(U(1)^f)$ down to $\text{sRep}(\mathbb{Z}_2^f)$ [48]. Thus, the resulting phase is a charge- $2e$ superconductor.

This categorical description of the FSHI-SC transition and resultant superconductor fully aligns with both the numerical results, e.g., the lack of spin Hall conductivity, and the field-theoretical analysis above.

VII. SUPERCONDUCTIVITY FROM DIFFERENT NON-ABELIAN FSHIS

a. The Pfaffian and Anti-Pfaffian States As written in the main text, the Pfaffian state is described by

$U(2)_{2,-4} \times U(1)_8$, whose Lagrangian is given by

$$\begin{aligned} \mathcal{L}_{\text{Pf}} &= -\frac{2}{4\pi} \text{Tr} \left(c \, dc + \frac{2}{3} c^3 \right) + \frac{3}{4\pi} (\text{Tr} \, c) \, d(\text{Tr} \, c) \\ &\quad + \frac{1}{2\pi} A \, d(\text{Tr} \, c) + \frac{1}{4\pi} A \, dA, \end{aligned}$$

where c is a $U(2)$ gauge field and A is the background electromagnetic gauge field. We also consider the anti-Pfaffian state is described by $[\text{SU}(2)_{-2} \times U(1)_8]/\mathbb{Z}_2$, with the Lagrangian [54],

$$\begin{aligned} \mathcal{L}_{\text{aPf}} &= \frac{2}{4\pi} \text{Tr} \left(c \, dc + \frac{2}{3} c^3 \right) - \frac{3}{4\pi} (\text{Tr} \, c) \, d(\text{Tr} \, c) \\ &\quad + \frac{1}{2\pi} A \, d(\text{Tr} \, c). \end{aligned}$$

b. The aPf \times $\overline{\text{aPf}}$ FSHI The Lagrangian describing $\text{aPf} \times \overline{\text{aPf}}$ is

$$\begin{aligned} \mathcal{L}_{\text{aPf} \times \overline{\text{aPf}}} &= \mathcal{L}_{\text{aPf}} + \mathcal{L}_{\overline{\text{aPf}}} \\ &= -\frac{2}{4\pi} \text{Tr} \left(c \, dc + \frac{2}{3} c^3 \right) + \frac{3}{4\pi} (\text{Tr} \, c) \, d(\text{Tr} \, c) \\ &\quad - \frac{1}{2\pi} A \, d(\text{Tr} \, c) \\ &\quad + \frac{2}{4\pi} \text{Tr} \left(c' \, dc' + \frac{2}{3} c'^3 \right) - \frac{3}{4\pi} (\text{Tr} \, c') \, d(\text{Tr} \, c') \\ &\quad + \frac{1}{2\pi} A \, d(\text{Tr} \, c'). \end{aligned}$$

Now, we condense the bifundamental field Φ that couples to the gauge fields as $D\Phi = \partial\Phi - ic\Phi - i\Phi c'$ so that $c = -c'$ is imposed in the low-energy regime. As a consequence, we get

$$\mathcal{L}_{\text{aPf} \times \overline{\text{aPf}}} \rightarrow -\frac{2}{2\pi} A \, d(\text{Tr} \, c).$$

Again, this is the effective field theory describing a charge-2 superconductor [31].

c. The Pf \times aPf FSHI We also note that superconductivity can emerge from $\text{Pf} \times \text{aPf}$. The Lagrangian describing $\text{Pf} \times \text{aPf}$ is

$$\begin{aligned} \mathcal{L}_{\text{Pf} \times \text{aPf}} &= \mathcal{L}_{\text{Pf}} + \mathcal{L}_{\text{aPf}} \\ &= -\frac{2}{4\pi} \text{Tr} \left(c \, dc + \frac{2}{3} c^3 \right) + \frac{3}{4\pi} (\text{Tr} \, c) \, d(\text{Tr} \, c) \\ &\quad + \frac{1}{2\pi} A \, d(\text{Tr} \, c) + \frac{1}{4\pi} A \, dA \\ &\quad + \frac{2}{4\pi} \text{Tr} \left(c' \, dc' + \frac{2}{3} c'^3 \right) - \frac{3}{4\pi} (\text{Tr} \, c') \, d(\text{Tr} \, c') \\ &\quad + \frac{1}{2\pi} A \, d(\text{Tr} \, c'). \end{aligned}$$

Now, we condense the matter field Φ that couples to the gauge fields through $D\Phi = \partial\Phi - ic\Phi + i\Phi c'$. In this case, the condensation imposes the constraint $c = c'$. As a result, we get

$$\mathcal{L}_{\text{Pf} \times \text{aPf}} \rightarrow \frac{2}{2\pi} A \, d(\text{Tr} \, c) + \frac{1}{4\pi} A \, dA.$$

This theory describes a charge-2 superconductor with chiral central charge $c_- = 1$ [30]. Note that this is consistent with expectation because Pf and aPf have $c_- = \frac{3}{2}$

and $c_- = -\frac{1}{2}$, respectively.

* These authors contributed equally to this work.

† gilyoungcho@kaist.ac.kr

- [1] Y. Jia, J. Yu, J. Liu, J. Herzog-Arbeitman, Z. Qi, H. Pi, N. Regnault, H. Weng, B. A. Bernevig, and Q. Wu, Moiré fractional chern insulators. i. first-principles calculations and continuum models of twisted bilayer MoTe₂, *Phys. Rev. B* **109**, 205121 (2024).
- [2] C.-E. Ahn, W. Lee, K. Yananose, Y. Kim, and G. Y. Cho, Non-abelian fractional quantum anomalous hall states and first landau level physics of the second moiré band of twisted bilayer MoTe₂, *Phys. Rev. B* **110**, L161109 (2024).
- [3] X.-W. Zhang, C. Wang, X. Liu, Y. Fan, T. Cao, and D. Xiao, Polarization-driven band topology evolution in twisted MoTe₂ and WSe₂, *Nature Communications* **15**, 4223 (2024).
- [4] F. Chen, W.-W. Luo, W. Zhu, and D. Sheng, Robust non-abelian even-denominator fractional chern insulator in twisted bilayer MoTe₂, *Nature Communications* **16**, 2115 (2025).
- [5] C. Xu, N. Mao, T. Zeng, and Y. Zhang, Multiple chern bands in twisted MoTe₂ and possible non-abelian states, *Phys. Rev. Lett.* **134**, 066601 (2025).
- [6] A. Abouelkomsan and L. Fu, Non-abelian spin hall insulator, *Phys. Rev. Res.* **7**, 023083 (2025).
- [7] M. Iskin, Extracting quantum-geometric effects from ginzburg-landau theory in a multiband hubbard model, *Phys. Rev. B* **107**, 224505 (2023).
- [8] S. A. Chen and K. T. Law, Ginzburg-landau theory of flat-band superconductors with quantum metric, *Phys. Rev. Lett.* **132**, 026002 (2024).
- [9] J.-X. Hu, S. A. Chen, and K. T. Law, Anomalous coherence length in superconductors with quantum metric, *Communications Physics* **8**, 20 (2025).
- [10] M. Iskin, Pair size and quantum geometry in a multiband hubbard model, *Phys. Rev. B* **111**, 014502 (2025).
- [11] M. Thumin and G. Bouzerar, Correlation functions and characteristic lengthscales in flat band superconductors, *SciPost Phys.* **18**, 025 (2025).
- [12] Q. Chen, Z. Wang, R. Boyack, S. Yang, and K. Levin, When superconductivity crosses over: From bcs to bec, *Rev. Mod. Phys.* **96**, 025002 (2024).
- [13] M. Oshikawa, Y. B. Kim, K. Shtengel, C. Nayak, and S. Tewari, Topological degeneracy of non-abelian states for dummies, *Annals of Physics* **322**, 1477 (2007).
- [14] Y. H. Kwan, G. Wagner, J. Yu, A. K. Dagnino, Y. Jiang, X. Xu, B. A. Bernevig, T. Neupert, and N. Regnault, Regarding the existence of abelian fractional topological insulators in twisted MoTe₂ and related systems, *Communications Physics* **9**, 10.1038/s42005-025-02483-6 (2026).
- [15] M. Oh, K. P. Nuckolls, D. Wong, R. L. Lee, X. Liu, K. Watanabe, T. Taniguchi, and A. Yazdani, Evidence for unconventional superconductivity in twisted bilayer graphene, *Nature* **600**, 240 (2021).
- [16] H. Tian, X. Gao, Y. Zhang, S. Che, T. Xu, P. Cheung, K. Watanabe, T. Taniguchi, M. Randeria, F. Zhang, C. N. Lau, and M. W. Bockrath, Evidence for dirac flat band superconductivity enabled by quantum geometry, *Nature* **614**, 440 (2023).
- [17] J. M. Park, Y. Cao, K. Watanabe, T. Taniguchi, and P. Jarillo-Herrero, Tunable strongly coupled superconductivity in magic-angle twisted trilayer graphene, *Nature* **590**, 249 (2021).
- [18] H. Kim, Y. Choi, C. Lewandowski, A. Thomson, Y. Zhang, R. Polski, K. Watanabe, T. Taniguchi, J. Alicea, and S. Nadj-Perge, Evidence for unconventional superconductivity in twisted trilayer graphene, *Nature* **606**, 494 (2022).
- [19] F. Xu, Z. Sun, J. Li, C. Zheng, C. Xu, J. Gao, T. Jia, K. Watanabe, T. Taniguchi, B. Tong, L. Lu, J. Jia, Z. Shi, S. Jiang, Y. Zhang, Y. Zhang, S. Lei, X. Liu, and T. Li, Signatures of unconventional superconductivity near reentrant and fractional quantum anomalous hall insulators (2025), [arXiv:2504.06972 \[cond-mat.mes-hall\]](https://arxiv.org/abs/2504.06972).
- [20] Y. Cao, V. Fatemi, S. Fang, K. Watanabe, T. Taniguchi, E. Kaxiras, and P. Jarillo-Herrero, Unconventional superconductivity in magic-angle graphene superlattices, *Nature* **556**, 43 (2018).
- [21] J. Wang, J. Cano, A. J. Millis, Z. Liu, and B. Yang, Exact landau level description of geometry and interaction in a flatband, *Phys. Rev. Lett.* **127**, 246403 (2021).
- [22] M. Fujimoto, D. E. Parker, J. Dong, E. Khalaf, A. Vishwanath, and P. Ledwith, Higher vortexability: Zero-field realization of higher landau levels, *Phys. Rev. Lett.* **134**, 106502 (2025).
- [23] Z. Liu, B. Mera, M. Fujimoto, T. Ozawa, and J. Wang, Theory of generalized landau levels and its implications for non-abelian states, *Phys. Rev. X* **15**, 031019 (2025).
- [24] D. Guerci, A. Abouelkomsan, and L. Fu, From fractionalization to chiral topological superconductivity in a flat chern band, *Phys. Rev. Lett.* **135**, 186601 (2025).
- [25] S. Maiti and A. V. Chubukov, Renormalization group flow, competing phases, and the structure of superconducting gap in multiband models of iron-based superconductors, *Phys. Rev. B* **82**, 214515 (2010).
- [26] J. González, Kohn-luttinger superconductivity in graphene, *Phys. Rev. B* **78**, 205431 (2008).
- [27] R. Nandkishore, L. S. Levitov, and A. V. Chubukov, Chiral superconductivity from repulsive interactions in doped graphene, *Nature Physics* **8**, 158 (2012).
- [28] G. Shavit and J. Alicea, Quantum geometric kohn-luttinger superconductivity, *Phys. Rev. Lett.* **134**, 176001 (2025).
- [29] E. Fradkin, C. Nayak, A. Tsvetlik, and F. Wilczek, A chern-simons effective field theory for the pfaffian quantum hall state, *Nuclear Physics B* **516**, 704 (1998).
- [30] Z. D. Shi, C. Zhang, and S. Todadri, Doping lattice non-abelian quantum hall states, *SciPost Phys.* **19**, 150 (2025).
- [31] T. H. Hansson, V. Oganesyan, and S. L. Sondhi, Superconductors are topologically ordered, *Annals of Physics* **313**, 497–538 (2004).

- [32] X.-G. Wen and Y.-S. Wu, Transitions between the quantum hall states and insulators induced by periodic potentials, *Phys. Rev. Lett.* **70**, 1501 (1993).
- [33] S.-P. Kou, J. Yu, and X.-G. Wen, Mutual chern-simons landau-ginzburg theory for continuous quantum phase transition of \mathbb{Z}_2 topological order, *Phys. Rev. B* **80**, 125101 (2009).
- [34] M. Barkeshli and X.-G. Wen, Anyon condensation and continuous topological phase transitions in non-abelian fractional quantum hall states, *Phys. Rev. Lett.* **105**, 216804 (2010).
- [35] M. Barkeshli and J. McGreevy, Continuous transition between fractional quantum hall and superfluid states, *Phys. Rev. B* **89**, 235116 (2014).
- [36] Z. Han, T. Wang, Z. Dong, M. P. Zaletel, and A. Vishwanath, *Anyon superfluidity of excitons in quantum hall bilayers* (2025), [arXiv:2508.14894](https://arxiv.org/abs/2508.14894) [cond-mat.str-el].
- [37] Z. Zhou, C. Wang, and Y.-C. He, *Chern-simons-matter conformal field theory on fuzzy sphere: Confinement transition of kalmeyer-laughlin chiral spin liquid* (2025), [arXiv:2507.19580](https://arxiv.org/abs/2507.19580) [cond-mat.str-el].
- [38] K.-W. Huang, X.-J. Hou, and Y.-H. Wu, *Third-order quantum phase transitions of bosonic non-abelian fractional quantum hall states* (2025), [arXiv:2509.17113](https://arxiv.org/abs/2509.17113) [cond-mat.str-el].
- [39] W. Ji, R. A. Lanzetta, Z. Zhou, and C. Wang, *Self-dual higgs transitions: Toric code and beyond* (2026), [arXiv:2601.20945](https://arxiv.org/abs/2601.20945) [cond-mat.str-el].
- [40] Y.-H. Wu, H.-H. Tu, and M. Cheng, Continuous phase transitions between fractional quantum hall states and symmetry-protected topological states, *Phys. Rev. Lett.* **131**, 256502 (2023).
- [41] S. Gazit, F. F. Assaad, S. Sachdev, A. Vishwanath, and C. Wang, Confinement transition of \mathbb{Z}_2 gauge theories coupled to massless fermions: Emergent quantum chromodynamics and $SO(5)$ symmetry, *Proceedings of the National Academy of Sciences* **115**, E6987 (2018).
- [42] T.-S. Zeng, D. N. Sheng, and W. Zhu, Continuous phase transition between bosonic integer quantum hall liquid and a trivial insulator: Evidence for deconfined quantum criticality, *Phys. Rev. B* **101**, 035138 (2020).
- [43] M. Schuler, L.-P. Henry, Y.-M. Lu, and A. M. Läuchli, Emergent xy^* transition driven by symmetry fractionalization and anyon condensation, *SciPost Phys.* **14**, 001 (2023).
- [44] K. Hwang, Anyon condensation and confinement transition in a kitaev spin liquid bilayer, *Phys. Rev. B* **109**, 134412 (2024).
- [45] T. Wang, X.-Y. Song, M. P. Zaletel, and T. Senthil, *Emergent qed_3 at the bosonic laughlin state to superfluid transition* (2026), [arXiv:2507.07611](https://arxiv.org/abs/2507.07611) [cond-mat.str-el].
- [46] A. M. Polyakov, Quark confinement and topology of gauge theories, *Nuclear Physics B* **120**, 429 (1977).
- [47] M. Teper, The confining string and its tension for $SU(2)$ gauge fields in $2 + 1$ dimensions, *Physical Letters B* **311**, 223 (1993).
- [48] D. Seo, T. Lee, and G. Y. Cho, *A unified categorical description of quantum hall hierarchy and anyon superconductivity* (2026), [arXiv:2602.03848](https://arxiv.org/abs/2602.03848) [cond-mat.str-el].
- [49] X.-G. Wen, A theory of $2+1d$ bosonic topological orders, *National Science Review* **3**, 68–106 (2015).
- [50] P. Bruillard, C. Galindo, T. Hagge, S.-H. Ng, J. Y. Plavnik, E. C. Rowell, and Z. Wang, Fermionic modular categories and the 16-fold way, *Journal of Mathematical Physics* **58**, 041704 (2017).
- [51] M. Barkeshli, P. Bonderson, M. Cheng, and Z. Wang, Symmetry fractionalization, defects, and gauging of topological phases, *Phys. Rev. B* **100**, 115147 (2019).
- [52] N. Seiberg and E. Witten, Gapped boundary phases of topological insulators via weak coupling, *Prog. Theor. Exp. Phys.* **2016**, 12C101 (2016).
- [53] T. Lan, L. Kong, and X.-G. Wen, Classification of $(2+1)$ -dimensional topological order and symmetry-protected topological order for bosonic and fermionic systems with on-site symmetries, *Phys. Rev. B* **95**, 235140 (2017).
- [54] P.-S. Hsin, Y.-H. Lin, N. M. Paquette, and J. Wang, Effective field theory for fractional quantum hall systems near $\nu = 5/2$, *Phys. Rev. Res.* **2**, 043242 (2020).